Diagenesis and reservoir quality evolution of the Lower Cretaceous turbidite sandstones of the Agat Formation (Norwegian North Sea): Impact of clay grain coating and carbonate cement

Fares Azzam, Thomas Blaise, Patricia Patrier, Ahmed Abd Elmola, Daniel Beaufort, Eric Portier, Benjamin Brigaud, Jocelyn Barbarand, Sylvain Clerc

Fares Azzam, Thomas Blaise, Patricia Patrier, Ahmed Abd Elmola, Daniel Beaufort, et al.. Diagenesis and reservoir quality evolution of the Lower Cretaceous turbidite sandstones of the Agat Formation (Norwegian North Sea): Impact of clay grain coating and carbonate cement. Marine and Petroleum Geology, 2022, 142, pp.105768. 10.1016/j.marpetgeo.2022.105768 . hal-04036744

Version of Record: https://www.sciencedirect.com/science/article/pii/S026481722200246X
Manuscript_0a829232a0948ecc789444036ff6f8af

Diagenesis and reservoir quality evolution of the Lower Cretaceous turbidite sandstones of the Agat Formation (Norwegian North Sea): Impact of clay grain coating and carbonate cement.

Fares Azzam [1*], Thomas Blaise [1], Patricia Patrier[2], Ahmed Abd Elmola[2], Daniel Beaufort[2], Eric Portier [3], Benjamin Brigaud [1], Jocelyn Barbarand [1], Sylvain Clerc [4]

[1] Université Paris-Saclay, CNRS, GEOPS, 91400 Orsay, France

[2] Université de Poitiers, IC2MP - UMR 7285 - CNRS, 86073, Poitiers, France

[3] CV Associes Engineering, Bayonne 64100, France

[4] Neptune Energy Norge AS, Vestre Svanholmen 6, 4313 Sandnes, Norway

* Corresponding author: Fares (First name) Azzam (Family name)

Primary e-mail: Fares.199@live.com

Secondary e-mail: Fares.azzam@universite-paris-saclay.fr

Highlights

- The Agat Formation experienced a complex and multistage diagenetic history.
- Thick-authigenic chlorite coats caused significant porosity loss in the reservoir.
- Chlorite formed through solid-state transformation from a berthierine precursor.
- Intense dissolution of feldspars and calcite cement improved the reservoir quality.
- Initial mineralogical composition mainly controlled the diagenetic processes evolution.

Abstract

The turbidite sandstone of the Agat Formation is one of the most important hydrocarbon reservoirs in the Lower Cretaceous succession of the Norwegian North Sea. The diagenetic history of these sandstones has greatly impacted the reservoir quality, resulting in a high heterogeneity in porosity and permeability. To investigate this impact, sixty thin sections and rock samples were investigated through petrographic observations, geochemical microanalysis, and X-ray diffraction. Three main diagenetic events occurred during burial and influenced the reservoir properties: (1) mutual growth of chlorite, siderite, and apatite, (2) calcite cementation, and (3) dissolution of K-feldspar and calcite. Early diagenesis occurs under strongly reducing conditions, leading to the formation of Fe-chlorite/berthierine, siderite, pyrite, and apatite forming coatings around the detrital grains. Chlorite coatings have a key role in controlling the reservoir quality in the Agat Formation. In the lower part of the reservoir, chlorite forms thick coats (15–25 µm) that strongly reduce permeability. Conversely, in the upper part of the reservoir, chlorite coats are thinner (4–10 µm), favoring porosity preservation by inhibiting quartz overgrowth. X-ray diffraction and electron microscope observations indicate Fe-rich chlorite of Ib polytype, suggesting solid-state transformation from a berthierine precursor. The kinetics of berthierine/chlorite growth are governed by the dissolution of Fe-rich grains and fine fraction materials found as matrix and early coats. These grains are abundant in the lower part of the reservoir favoring the formation of thick chlorite coats. Chlorite was followed by pervasive calcite cementation in deep burial conditions creating low permeability barriers in the reservoir. The source of this calcite is internal and probably related to the dissolution of an early diagenetic calcite cement forming at shallow depth, with a minor contribution from marine carbonates. During late diagenesis, K-feldspar grains and calcite cements underwent intense dissolution creating secondary porosity and consequently increasing permeability. The input of acidic fluids associated with the maturation of the source rocks could have facilitated these dissolution reactions. Our results highlight the importance of inherited mineralogy in controlling the distribution of chlorite, carbonates, and secondary porosity in the Agat Formation. This study provides useful indicators to help predict diagenetic reactions that can occur in deep marine siliciclastic reservoirs.

Keywords: Sandstone, Diagenesis, Reservoir, Hydrocarbon, Turbidites, Chlorite coat, Carbonate cement, North Sea

1. Introduction

In many hydrocarbon fields, reservoir properties are strongly linked to diagenetic reactions occurring during burial. These reactions can either positively or negatively affect the quality of sandstone reservoirs (Worden and Burley, 2003). In some cases, the development of some early diagenetic minerals can preserve the reservoir quality when the sediments are subjected to increasing burial and temperature. For example, Fe-chlorite is a common diagenetic mineral in old marine sandstone generally found as grain coating (Worden et al., 2020 and references therein). Over the last few years, several studies have shown a close relationship between porosity preservation in deeply buried sandstone and the presence of chlorite coats around detrital grains (Billault et al., 2003; Bloch et al., 2002; Ehrenberg, 1993; Hansen et al., 2021; Houseknecht and Ross, 1992; Saïag et al., 2016; Virolle et al., 2022). Laboratory experiments simulating quartz cementation have demonstrated that chlorite crystals coating detrital grains can block early quartz overgrowth (e.g., Ajdukiewicz and Larese, 2012). By inhibiting extensive quartz cementation, porosity can be preserved up to a high burial depth (Ehrenberg, 1993). Similarly, carbonate cements can significantly influence the quality of sandstone reservoir by forming barriers to fluid flows (Prosser et al., 1993; Xiong et al., 2016). However, early diagenetic calcite cements can preserve the inter-granular volume (IGV) by delaying burial compaction, which may lead to high porosity upon dissolution (Estupiñan et al., 2007; Liu et al., 2014; Xiong et al., 2016).

The origin of diagenetic chlorite and carbonates in deep marine sandstone has not been widely explored and has received less attention than those from a shallow marine environment (Dowey et al., 2012; Hendry et al., 1996; Yezerski and Shumaker, 2018). To address these gaps, this study explores the diagenesis in the turbidite sandstone of the Agat Formation (Fm), one of the most important sandstone reservoirs in the Lower Cretaceous succession in the northern North Sea (Copestake et al., 2003). The Agat Fm consists of massive and deep-sea turbiditic sands deposited through gravity flow turbidity currents at the outlet of canyons incised within the continental shallow marine platform (Hansen et al., 2021). Although the sedimentological features of this formation are well documented (Bugge et al., 2001; Hansen et al., 2021; Lien et al., 2006; Nystuen, 1999; Shanmugam, 1995; Skibeli et al., 1995), its diagenetic evolution has not been widely explored. The recent study by Hansen et al. (2021) highlighted the role of chlorite coats in controlling the reservoir quality of the Agat Fm. The study also suggested that chlorites were the result of the replacement of detrital clay precursors. In this contribution, we go further by discussing the origin of the clay precursor and the timing of the chloritization process. In addition to chlorite, carbonate cements are reported in many North Sea reservoirs, including the Agat Fm (Saigal and Bjørlykke, 1987). However, the source of carbonates and their spatial distribution within the reservoirs are not fully understood (Morad, 1998).

Therefore, the main objectives of this paper include the following:

1. Reconstruct the diagenetic history of the Agat Formation.
2. Trace the source of chlorite and carbonate cements.
3. Identify the origin of early detrital clay precursors in deep marine sands and the processes that control their transformation into continuous and well-crystallized chlorite coatings.
4. Assess the effect of diagenesis on the Agat Fm reservoir quality.
5. Build a reliable geological and diagenetic model to predict the distribution of chlorite coats and carbonate cements in turbidite deposits.

Addressing these objectives will offer a better understanding of the key parameters that control chlorite and carbonate distribution in turbidite deposits. A prediction model of the reservoir quality based on these parameters could help unlock many deepwater plays elsewhere.

2. Geological settings

The study area is located in the northeastern part of the North Sea, about 35 kilometers from the shore of Norway and 6 kilometers from the Gjøa oilfield (Fig. 1A). Lying within the Måløy Terrace, it is bounded to the east by the Øygarden fault complex and to the west by the normal fault of the eastern margin of Sogn Graben (Fig. 1A). The Cretaceous period in the North Sea is regarded as a time of thermal subsidence following the major rifting phase of the Middle to Late Jurassic, which created a series of under-filled rifts and sub-basins (Glennie, 2009).

The Cretaceous succession in the Northern North Sea is dominated by the deposition of fine-grained lithologies (offshore marls and mudstones) from suspension settling (Fig. 1B) (Isaksen and Tonstad, 1989). The sediments are transgressive, recording an overall deepening in the basin (Ziegler, 1975). However, this period was interrupted by several regressive events during Aptian-Albian times and during the late Turonian that were related to the culmination of Austrian tectonic activity (Crittenden et al., 1998; Oakman and Partington, 1998; Ziegler, 1992, 1975). These events locally resulted in the remobilization and deposition of coarse siliciclastic sediments in deep sub-basins. During the Aptian-Albian times, gravity flows on the Måløy Slope created a series of slopes and basin floor sand systems known as the Agat Fm (Bugge et al., 2001; Jackson et al., 2008; Skibeli et al., 1995). These slope systems were sourced from the east, from a relatively small source area (5000-8000 km^2), and the adjacent paleoshelf was relatively narrow (20-30 km wide) (Bugge et al., 2001; Hansen et al., 2021; Jackson et al., 2008; Martinsen et al., 2005). The Agat Fm was deposited at the base of a fault-related slope that was cut by several incised canyons. The sedimentary materials was mainly derived from the remobilization and reworking of shallow marine sands (Hansen et al., 2021; Martinsen et al., 2005). The Agat Fm is a stratigraphic pinch-out trap in upper slope settings (Shanmugam et al., 1994). The massive sand reservoir inter-fingers within the shales or marls of the Rødby Fm, acting as a seal (Fig. 1B). The primary source rocks identified in the study area are the Upper Jurassic organic-rich shale (Draupne and Heather Formations) and the Lower Jurassic shales of the Ness Formation (Goff, 1984).

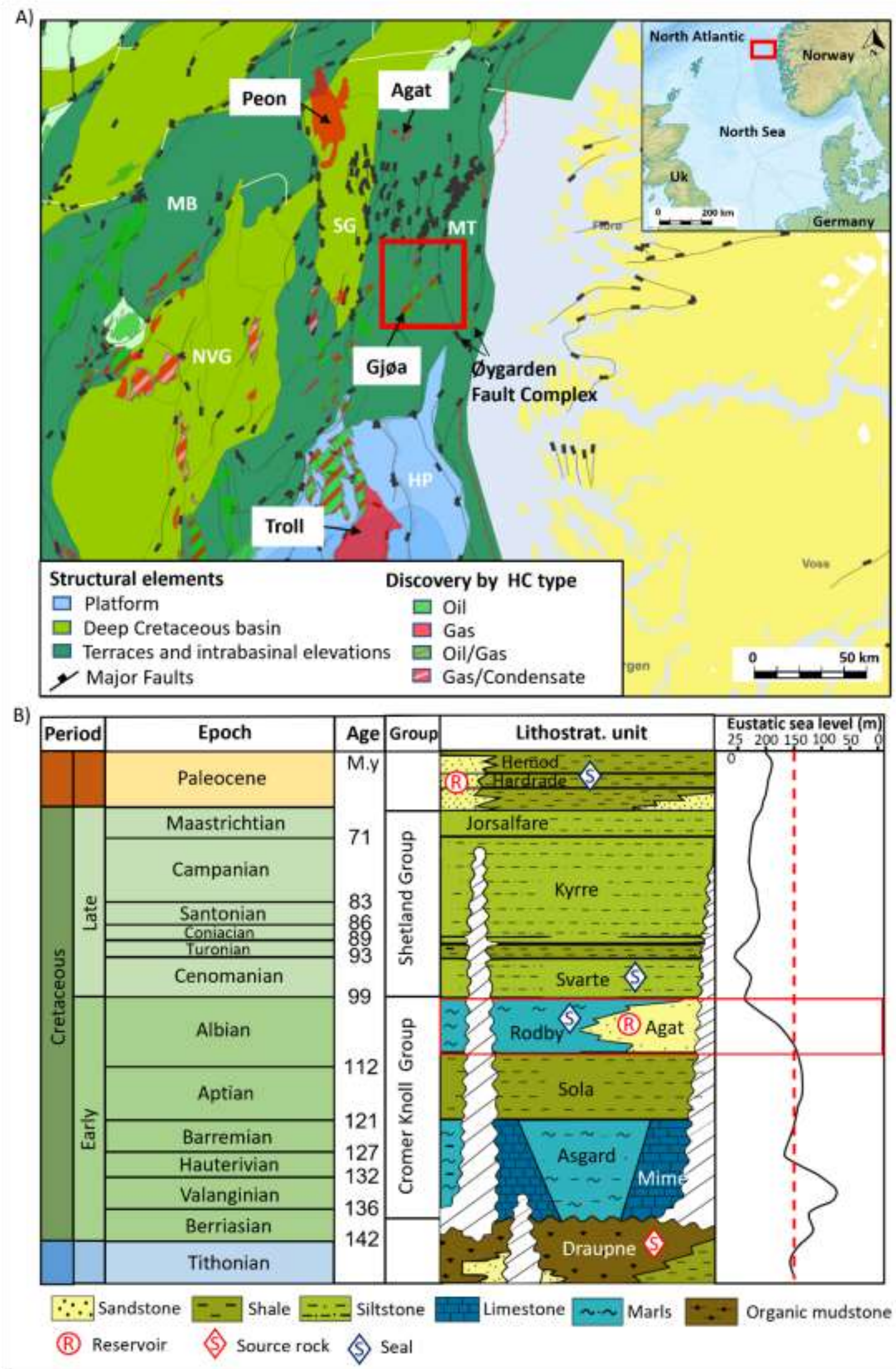

Fig. 1. (A) Simplified map showing the location of the study area indicated by a red square with the main structural elements of the northern North Sea. MB: Marulk Basin; NVG: North Viking Graben; SG: Sogn Graben; HP: Horda platform; MT: Måløy Terrace. The structural map is edited from the Norwegian Petroleum Directorate (NPD) website www.npd.no; (B) Cretaceous stratigraphy of the Northern North Sea (Gradstein et al., 2016) combined with the eustatic sea-level curve of Haq (2014).

2.1. Well logs and petrophysical properties

A summary of well log data (GR, RHOB, NPHI, Vshale), lithology, porosity, and permeability measurements is presented in Figure 2. The Agat Fm in the study area has a thickness of about 118 m. The reservoir interval is divided into two parts, mainly based on the reservoir quality and the sand-shale ratios. The volume of shale (Vshale) is mainly due to the presence of chlorite (Hansen et al., 2021). The upper part (hereafter called Upper Reservoir (UR)) comprises the “Upper Reservoir 1 (UR 1)” mainly composed of heterolithic sediments with interstratification of mudclast layers (Vshale 7 % - 45 %), and the “Upper Reservoir 2 (UR 2)” mainly composed of clean structureless sandstone with high visual porosity and low shale content (Vshale < 7 %). The reservoir quality of the UR is very good, displaying a permeability that ranges from 95 mD to 12400 mD and helium porosity that ranges from 17.6 % to 30.5 %. The lower part (hereafter called Lower Reservoir – (LR)) consists of multiple fining upward sequences composed of sand with a volume of shale ranging from 10 % up to 25 %. The reservoir quality of the LR is weak to moderate, displaying a permeability that ranges from 0.15 to 50 mD, and helium porosity that ranges from 8.2 % to 28.5 %.

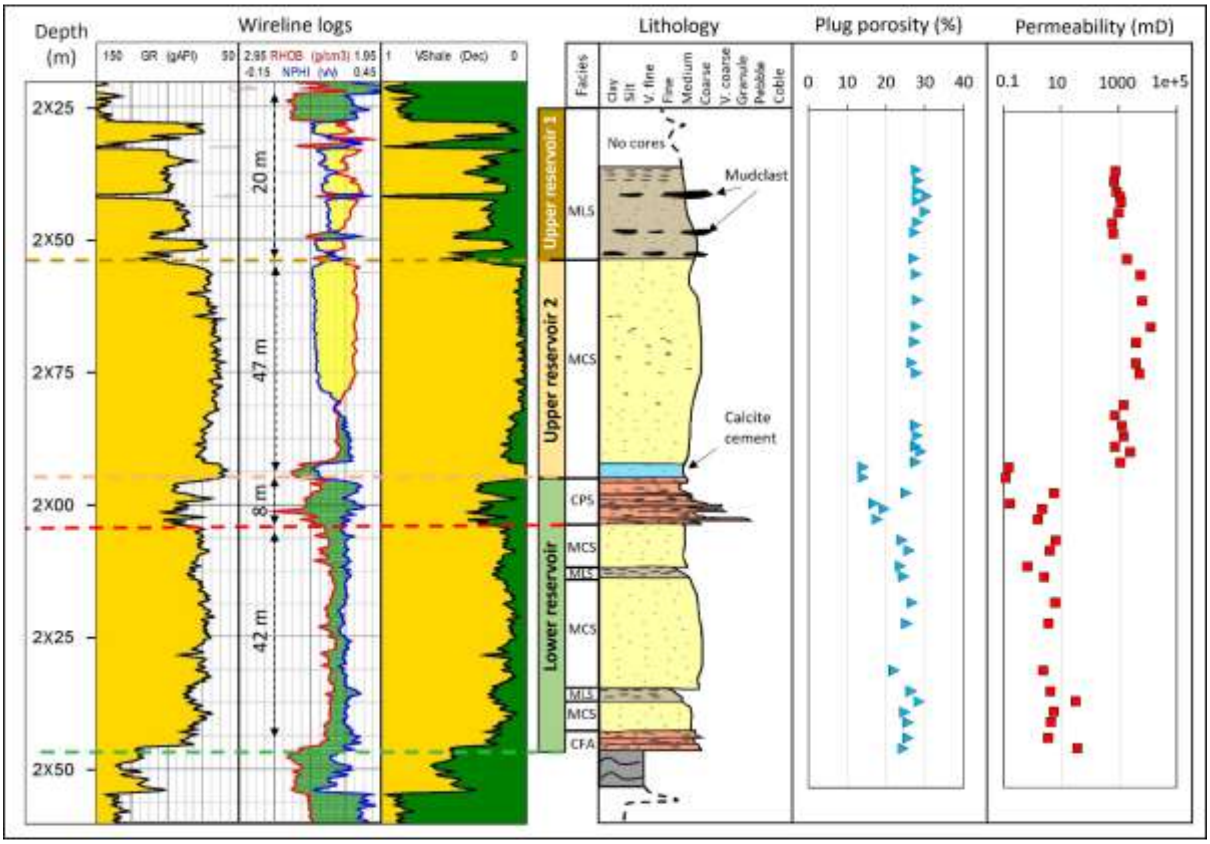

Fig. 2. Combination of wireline logs (Gamma Ray (GR), density-neutron (RHOB-NPHI), and Volume shale (Vshale)) along with core plug porosity and permeability and the lithology log showing the location of the main facies in the studied well.

2.2. Sedimentology

Many sedimentological models have been proposed for the Agat Fm over the last few years. Shanmugam et al. (1994) and Skibeli et al. (1995) first suggested deposition from slumping and debris flows in upper-slope settings. However, recent studies have described the Agat Fm as the result of gravity flow turbidity currents (Bugge et al., 2001; Lien et al., 2006; Nystuen, 1999). This interpretation was recently confirmed by Hansen et al. (2021), suggesting a deposition from high-density turbidity currents from the remobilization of shallow marine sands.

Four main facies are identified in the Agat Fm in the study area (Hansen et al., 2021): (1) Massive clast-rich sandstone facies (MCS), which form most of the sandstone interval. These facies consist of a thick, continuous interval of clean sandstone, generally massive and structureless, moderately to well-sorted, medium to coarse-grained, and containing dispersed lithic/clast materials (Fig. 3A). The lack of stratification in these facies suggests rapid deposition from multi-events of large-volume concentrated flows. The absence of structure may be due to dewatering and homogenization. (2) Massive-laminated sandstone facies (MLS) generally comprises stratified pebbly and non-pebbly sandstone that are moderate to well-sorted, locally clean, and fine to medium-grained, which overall fining upwards. Planar stratification or lamination is defined by concentrations of pebbles and mudstone or carbonaceous-mudstone grains (Fig. 3B). These facies record high-concentration, wanning tractional grain-flows which gradually decreased in energy through time. This is interpreted as hybrid beds with a raft of siltstones to mudstones formed at the transition of scour channel-lobe transition. (3) Conglomeratic-pebbly sandstone facies (CPS) that consists of several meters of granule and pebble-grade conglomerate beds intercalated with moderately to poorly sorted, medium to coarse-grained sandstone. Greenish clay grains are highly abundant, as well as mud clasts and some phosphatic and siderite clasts (Fig. 3C). These sediments are probably derived from a tractional transport of various clasts within relatively low volume, high energy, episodic flows. (4) Chaotic facies association (CFA) forming the base of the Agat Reservoir consists of a 3-meter-thick assemblage of poorly sorted large mudstone clasts in a silty matrix or in fine-grained sandstone (Fig. 3D). The clasts are likely to be derived from the erosion of the Rodby Formation (middle Cretaceous shale). These chaotic facies correspond to oliostrome deposits (slide and slump complex) that accumulate as a semifluid body by submarine gravity sliding or the slumping of the unconsolidated sediments (Abbate et al., 1970). Their deposition at the base of the turbiditic sequence is probably related to a period of submarine canyon/channel incision prior to the establishment of the Agat Fm.

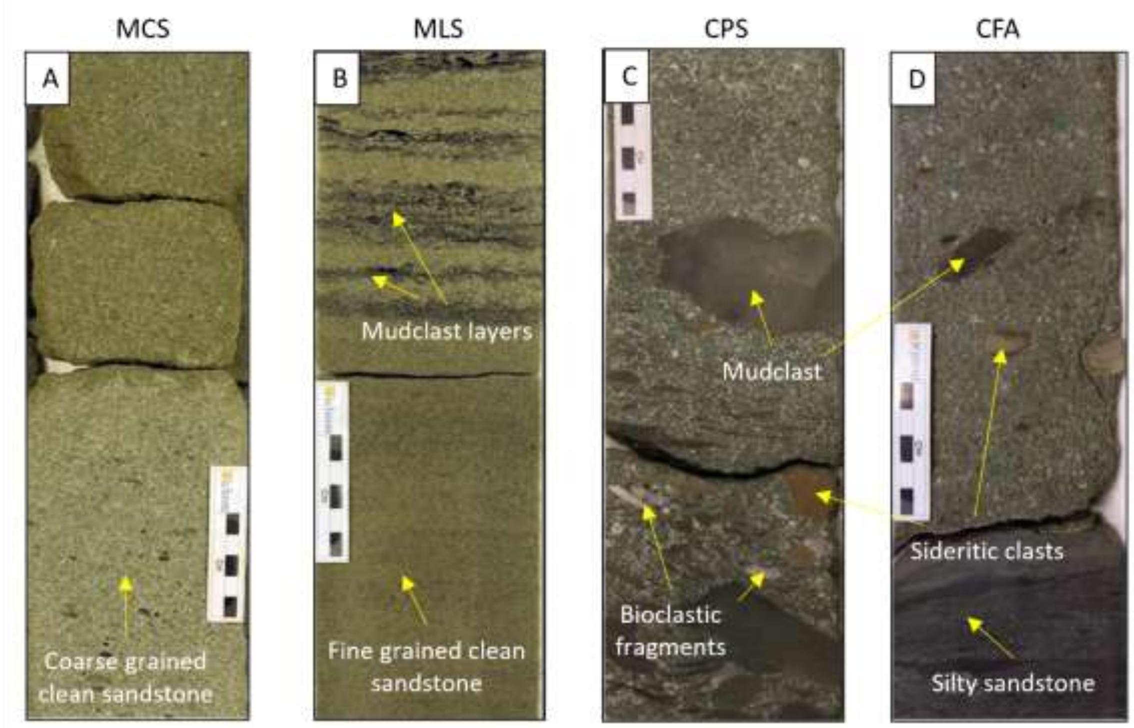

Fig. 3. Major sedimentary facies in the Agat Fm: (A) Clean structureless coarse-grained sandstone; (B) Planar stratified fine-grained sandstone. Stratification is defined by ~~concentrations of~~ mud-clast layers at the top of the sandstone sequence; (C) Beds of poorly and moderately sorted pebbly sandstone containing angular fragments of dark grey mudstone and sub-rounded brown sideritic clast. Some bioclastic fragments are also present; (D) Pebbly sandstone with large mud-clast and sideritic concretions in contact with highly silty, pebbly sandstone. MCS: Massive clast-rich sandstone; MLS: Massive-laminated sandstone; CPS: Conglomeratic-pebbly sandstone; CFA: Chaotic facies association.

3. Materials and Methods

All samples are provided by Neptune energy A/S, together with petrophysical data of well logs and core description reports. Well name and depth will be anonymized for confidentiality purposes. A total of 67 core plugs were collected from one well in the study area with a sampling interval ranging from 1 m to 2 m. Sixty samples were thin sectioned and polished for the petrographic examinations. The thin sections were impregnated with blue epoxy. Samples that contain carbonate cement were stained with alizarin-potassium ferricyanide. The burial history curve of the study area was reconstructed using PetroMod 1D ©.

3.1. Optical, cathodoluminescence, and scanning electron microscopy

A Leica DM750P polarizing petrographic microscope was used to observe thin sections under different magnifications. A composite microphotograph was created from a set of overlapping images for each thin section and then point-counted 250 times using Jmicrovision® software

(Roduit, 2007). Additionally, the size of approximately 300 grains was measured along their longer axis. Data were then imported to Gradistat © Simon Blott, a software calculating the grain size distribution, skewness, and sorting (Blott and Pye, 2001). Sphericity and roundness were visually defined following the chart of Krumbein (1963). The type of grain-to-grain contact and the intensity of compaction were described for each sample using the methods of Taylor (1950). All thin sections containing carbonate cement were examined under cathodoluminescence microscopy (OPEA cathodyne 12 keV, 200 mA). Scanning Electron Microscopy (SEM) observations were carried out using a Phenom mini-SEM benchtop (10 keV in imaging mode and 15 keV for elementary analyses) equipped with an Energy-Dispersive X-ray spectroscopy analyzer (EDS).

3.2. X-ray diffraction analysis

The bulk and clay mineralogy of the sandstone were obtained using a PANalytical X'Pert–Pro diffractometer with a Cu anticathode ($K\alpha 1=1.5405$; 45 kV; 40 mA) at Geosciences Paris-Saclay (GEOPS) laboratory. X-ray diffraction (XRD) of randomly oriented powder mounts was conducted on thirty representative samples to characterize the ~~whole~~ bulk mineralogy based on d_{hkl} reflections. The diffractograms were acquired between 2 and 65°2θ at a step size of 0.02°2θ and acquisition time of 1 s. Semi-quantitative estimates of the mineral phases from X-ray diffraction data were carried out using Rietveld refinement with X'Pert HighScore © PANalytical software.

To identify the clay mineralogy according to their d_{00l} reflections, X-ray diffractograms of oriented preparations (< 2µm fraction size) were acquired in air-dried conditions (AD). The presence of expandable clay minerals was checked using solvation with ethylene glycol (EG). The clay fraction was separated by sedimentation for 15 representative samples using the protocol of Brown and Brindley (1980) and Moore and Reynolds (1997). First, the samples were crushed and then placed in an ultrasonic beaker to ensure a correct dispersion of clay minerals. The samples were then treated with oxygen peroxide and hydrochloric acid to remove organic matter and carbonates. The clay fraction (<2 µm) was then extracted by collecting the first 2 cm after 1h 40 min of sedimentation. X-ray diffractograms of oriented sample preparations were acquired between 2 and 27°2θ at a step size of 0.01°2θ and acquisition time of 0.5 s per step. In addition, the peak positions of the d_{060} reflection on randomly oriented <2 µm fraction were acquired between 57–63° 2θ with a step size of 0.025° 2θ per 8 s counting time.

3.3. Electron microprobe analysis

The chemical composition of carbonates was determined using an Electron Probe Microanalyzer (EPMA) at the Sorbonne University, Paris. Thin sections were carbon-coated prior to the analysis. The accelerating voltage was 25 kV, the sample current was 20 nA, and the spot size was 5 µm. The proportions of all elements (Fe, Mn, Mg, Ca, Sr, C, and O) were normalized to 100 mol % for all samples. For these calculations, oxygen and carbon were determined by stoichiometry.

3.4. Laser ablation inductively coupled plasma mass spectrometry

The rare earth elements (REE) concentration in calcite and siderite cement were measured directly on thin sections using a sector field inductively coupled plasma mass spectrometer coupled to a laser ablation sampling system (LA-SF-ICP-MS) at GEOPS laboratory. Elemental concentrations were calibrated using NIST614 glass reference material, and the carbonate pellet MACS-3 (United States Geological Survey (USGS)) was used as a secondary reference material to ensure accuracy. The laser beam diameter for unknown calcite and calcite reference material MACS-3 was 85 µm (50 µm for siderite). Unknown calcites and siderite were ablated at a frequency of 10 Hz and a fluence of 2 J.cm^{-2}. ^{43}Ca was used as an internal standard, with a calcite CaO content of 54 wt.% and siderite CaO content of 1.9 wt.% based on EPMA measurements. The REE distributions were obtained by normalizing to the Post-Archean

Australian Shale (PASS) (McLennan, 2001). La, Ce, Eu, and Gd anomalies were calculated according to Lawrence et al. (2006). For some representative bulk rock samples, the REE concentration was measured by inductively coupled plasma mass spectrometry following pulverization and dissolution at ALS Minerals laboratory in Loughrea, Ireland.

3.5. In situ $\delta^{13}C$ and $\delta^{18}O$ microanalysis by SIMS

The isotopic composition of carbonates and quartz overgrowth was measured by Secondary Ion Mass Spectrometry (SIMS) using a Cameca IMS 1270 at the CRPG laboratory, Nancy, France. Thin sections were cleaned with absolute ethanol to remove any contamination and were gold-coated prior to the analysis. In carbonates, the oxygen and carbon stable isotope compositions were measured separately in two sessions using the same experimental conditions. $\delta^{18}O$ in quartz overgrowth was measured in a single analytical session. All samples were sputtered with a 10 kV Cs+ primary beam of 5 nA, focused on ~10 to 15 μm spots. The crater depth was <1 μm. Secondary negative oxygen ions were accelerated at 10 kV and analyzed at a mass resolution of about 5000 using the circular focusing mode of the IMS 1270 and a transfer optic of 150 μm. For calcite, the instrumental fractionation was determined prior to each session using a calcite reference material (CCcigA) with a value of 18.94 ‰ V-SMOW for $\delta^{18}O$ and 1.04 ‰ V-PDB for $\delta^{13}C$. For siderite, the instrumental fractionation was determined using a siderite crystal reference material (Ivigtut) with a $\delta^{18}O$ value of 9.1 ‰ V-SMOW and a $\delta^{13}C$ of –7.6 ‰ V-PDB. For quartz, the instrumental fractionation was determined using an internal reference material (Brésil2) with a $\delta^{18}O$ value of 19.62 ‰ V-SMOW. The homogeneity of the standard was checked by multiple measurements for various profiles. The instrument stability was checked during each session by carrying out 5 analyses on the reference material every 2 hours approximately. No instrument drift was observed in either session.

3.6. Microthermometry of fluid inclusions

Three polished wafers (200 μm thick) were prepared for fluid inclusion analysis within calcite cement to determine their minimal trapping temperature (Th) and the final melting temperature (Tm = solid ice phase into liquid phase). Fluid inclusions were first observed under transmitted light at high magnification to determine their nature and type. Fluid inclusion microthermometry was conducted using a Linkam THMSG600 heating freezing stage. Calibration was carried out using synthetic supercritical H_2O and H_2O-CO_2 fluid inclusions.

4. Results

4.1. Bulk mineralogical composition of the Agat Formation

The whole-rock XRD analysis of the Agat Fm shows close bulk mineralogy between the UR and the LR (Fig. 4 and Fig. A1 in Appendix). The samples are composed mainly of quartz, feldspar (K-feldspar and minor Na-feldspar), chlorite, and mica/glauconite in varying proportions. Semi-quantification of mineral phases from XRD shows that chlorite is mainly concentrated in the LR, and less abundant in the UR (Fig. 4). A similar trend is also observed for mica/glauconite, which are more abundant in the LR. Anatase, zircon, halite, and sylvite are present only in few samples. The presence of halite and sylvite in the samples is due mainly to the brine used in the drilling fluids. Pyrite is mainly observed in the UR 1, particularly in the MCS facies, where mud clasts are abundant. Calcite and siderite are generally found at the boundary between the UR and the LR (i.e., at the base of the UR and the top of the LR).

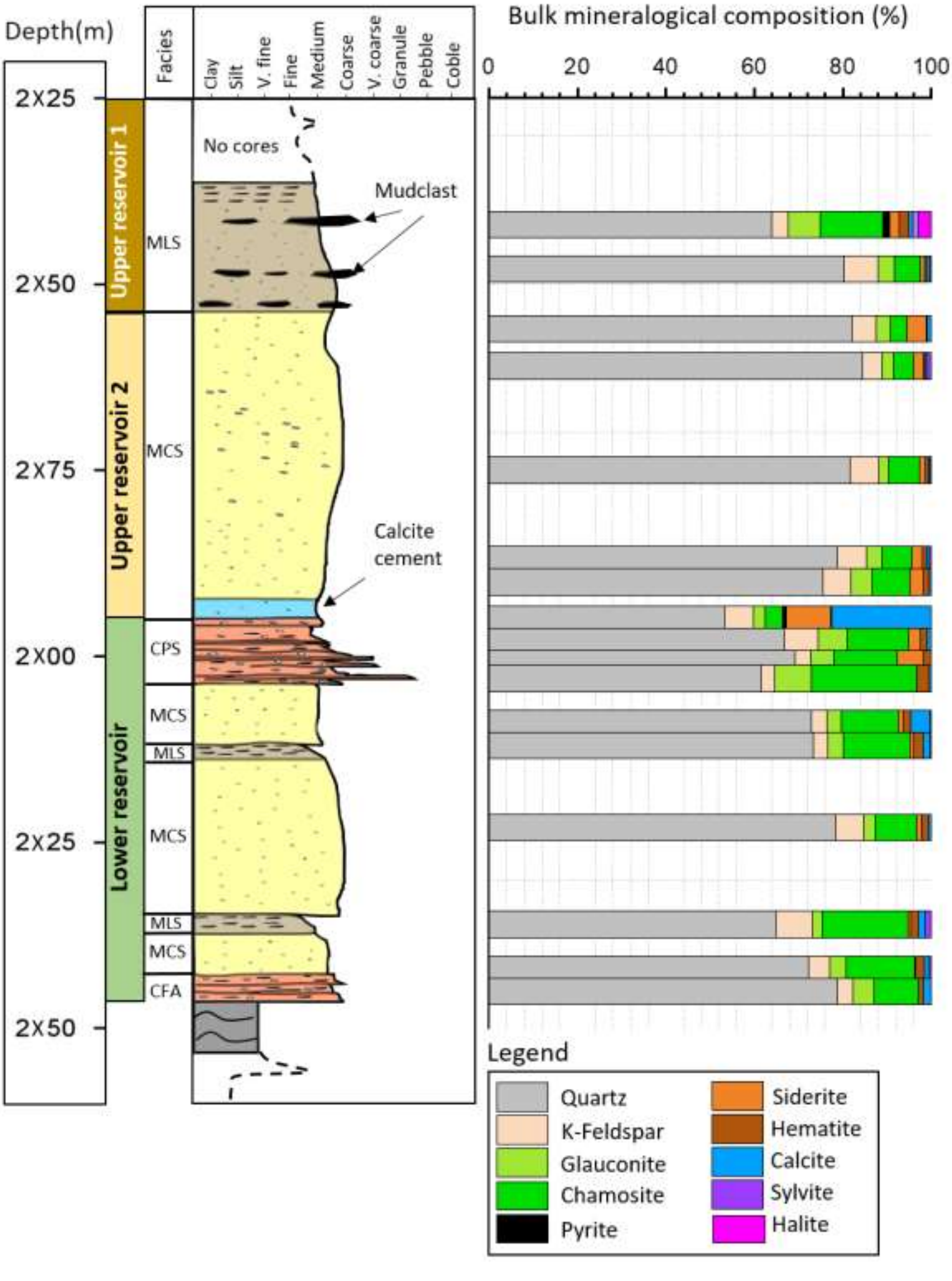

Fig. 4. A semi-quantification of the bulk mineralogical composition from X-ray diffraction using Rietveld refinement. It shows dominance of quartz and K-feldspars in the UR and a strong increase of chloritic and glauconitic clay minerals in the LR. Carbonate cements are mainly found at the limit between the UR and LR.

4.2. Grain composition

Petrographic observations show that the sand grains are mainly composed of quartz (24 % to 46 %) and lithic rock fragments (5 % to 21 %) associated with K-feldspar (3 % to 10 %) (Table 1). Quartz grains are mainly monocrystalline (av. ~27 % in UR and ~20 % in LR) with subordinate polycrystalline (av. ~10 % in UR and ~13 % in LR). Feldspar is mainly composed of orthoclase (av. ~7 % in UR and ~3% in LR) and a small amount of microcline (< 0.5 %). Lithics (av. ~13 % in UR and ~18 % in LR) are mostly composed of metamorphic fragments, but locally igneous and sedimentary rock fragments were observed in a small amount (<0.5 %). The metamorphic rock fragments are composed of polycrystalline quartz and some micas showing schistose patterns suggesting a high-grade metamorphic origin. Using the quartz-feldspar-lithic (QFL) ternary diagram classification of Folk (1980), most of the samples fall in the litharenite and feldspathic litharenite domains (Fig. 5). The framework composition of the Agat Fm is more homogeneous in the UR than in the LR. The latter contains more lithic fragments but less quartz and feldspar grains than the UR, reflecting a change in sediment provenance.

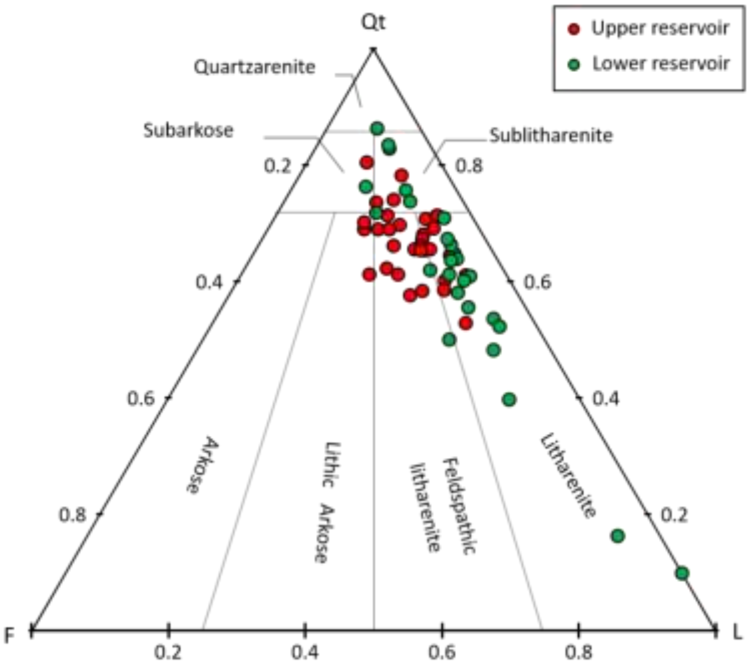

Fig. 5. QtFL (Quartz total – Feldspar – Lithics) ternary diagram of sandstone populations from the Agat Fm coded with reservoir division.

The ductile framework of the Agat Fm is mainly composed of glauconite-like grains, chlorite ooids/peloids, and ductile lithic fragments. On average, the ductile content in the UR is about 14.9 %, while the LR has more than 24.5 % of ductile grains. The glauconite-like grains are comparable in size to the associated quartz grains. These grains generally display an expanded vermicular shape with rounded abrasive edges, probably due to transport (Fig. 6A). Under cross-polarized light, they show similar extinction and birefringence to mica. A small proportion of discrete grains display typical habits of glauconite grains, generally showing a globular shape (Fig. 6B). Chlorite ooids and peloids are found as discrete spherical grains. These grains show fractures, abrasive edges, traces of heavy minerals, and micro quartz, indicating detrital origin. The ooids typically display concentric laminae with a nucleus consisting of fine matrix or heavy minerals (Fig. 6C), while peloids show massive structureless shapes composed uniformly of chlorite (Fig. 6D). Ductile lithic fragments are derived from sedimentary fragments like claystone and siltstone and igneous rock fragments containing small grains of quartz, feldspar, and biotite. In some samples, ductile grains and lithic fragments have undergone intense mechanical compaction, forming a pseudo-clayey matrix (Fig. 6E) which strongly reduces the porosity and permeability.

Table 1. Average point counting results of detrital mineralogy, authigenic mineralogy, and porosity for the main facies in the Agat Fm (N: number of samples, T: Thickness, Mo-Qz: Monocrystalline Quartz, Po-Qz: Polycrystalline Quartz, TQz: Total quartz, LF: Lithic Fragments, K-Felds: K-Feldspar, GP: Glauconite pellet, VG: Vermicular Glauconite, B-M: Biotite-Muscovite, Pfc: Porefilling chlorite, Cc: Chlorite coat, Sid: siderite, Ox: oxide, Ap: Apatite: Cal: calcite, Pp: Primary porosity, Sp: Secondary porosity, Tp: Total porosity).

		Detrital Mineralogy								Authigenic Mineralogy						Porosity		
Unit	Facies	Mo-Qz	Po-Qz	TQz	K-Felds	LF	GP	VG	B-M	Pfc	Cc	Sid	Ox	Ap	Cal	Pp	Sp	Tp
Upper	MLS (N=12, T~20 m)																	
	Min	19,4	5,7	32,8	3,2	5,1	1,2	1,6	0	1,2	2,7	0	0	0	0	4,4	3,7	10,3
	Mean	28,5	11,1	39,6	7,5	9,2	5,1	6,6	1,2	6,1	4,5	0,7	0,9	0	0	13,1	5,4	18,6
	Max	40,4	17,2	46,7	11,8	11,7	8	9,1	2,8	33,6	9,2	2,4	1,6	0,4	0	16,9	8,6	23,2
	SD	5,4	4,4	4,2	2,5	2	1,9	2,3	0,8	8,9	1,9	0,8	0,5	0,1	0	3,7	1,4	3,4
	MCS (N=17, T~47 m)																	
	Min	17,6	6,4	30,1	3,2	10,8	1,2	1,2	0	0,4	2	0,5	0	0	0	0	0,5	0
	Mean	25,2	13,5	38,8	6,1	15,5	4,5	3,9	0,3	3,8	4,9	2,8	0,4	0	2,9	11,9	5,5	16,8
	Max	32,5	20,4	44,4	10	23,6	9,4	7,6	1,6	10,8	7,2	9,8	1,2	0,5	20,3	17,6	9,5	25,7
	SD	3,1	4,3	4,1	1,8	3,2	2,2	1,6	0,4	2,5	1,9	2,4	0,4	0,1	7,3	4	2,6	6,8
Lower	CPS (N=7, T~8 m)																	
	Min	17,3	7,9	25,9	2,4	3,2	3,6	5,6	0	0,8	2,8	0	0,4	0	0	0	1,1	2,7
	Mean	23,1	10,8	33,9	3,7	12,7	10,1	9,1	0,3	8,9	10,2	4	0,7	0,5	1	1,5	3,8	5,3
	Max	33,1	19,5	43,8	7,2	20,9	16,7	15,6	0,4	36,3	18,7	14,7	1,6	2,5	4	3,5	7,2	9,2
	SD	5,5	4,3	7,3	1,6	6,7	4,1	4,1	0,2	12,5	6	5,7	0,4	0,9	2	1,4	2,4	2,6
	MCS (N=14, T~36 m)																	
	Min	16,5	4	24,5	2,3	4,4	3,5	3,5	0	0,8	2,8	0,4	0	0	0	0	1,6	1,3
	Mean	22,4	10,6	33	3,8	17,1	6,5	7,7	0,3	3,3	16,2	2,3	0,6	0,1	6,4	2,1	3,9	5,7
	Max	30,8	16,6	41,1	6,4	30,8	11,9	10,7	0,8	7,4	21,1	15	2,4	0,4	30,4	4,4	5,3	9,2

SD	4,4	3,9	5,4	1,2	6,8	2,6	2	0,3	2	5,4	4	0,6	0,2	12,1	1,2	1,1	2,3
MLS (n=3, T~4 m)																	
Min	22,1	10,7	35,4	6,2	8,4	3	5	0	7	16,2	0	0,4	0	0	1,1	1,7	3,5
Mean	26,6	12	38,6	7,1	12	5,8	6,3	0,3	8,1	16,9	0,2	0,4	0	0	1,5	2,8	4,3
Max	31,1	13,3	41,7	8	15,6	8,5	7,6	0,6	9,1	17,5	0,4	0,4	0	0	1,8	3,9	5
SD	6,3	1,9	4,5	1,3	5,1	3,9	1,8	0,4	1,5	0,9	0,3	0	0	0	0,5	1,6	1
CFA(n=3, T~3.7 m)																	
Min	21,7	9,8	31,5	3,5	5,2	3,6	8,7	0,4	2	6,8	0	0,3	0	0	1	3,5	5,4
Mean	23,5	12	35,5	5	13,9	5,9	10,3	0,6	7,8	9,6	0,3	0,4	0,1	2,6	3	4,4	7,4
Max	2,6	3,3	3,6	1,4	7,5	2,5	2,3	0,2	7,6	3,6	0,3	0,2	0,2	3,3	2,1	0,9	1,8
SD	26,5	15,7	38,2	6,3	19,1	8,6	12,9	0,7	16,4	13,7	0,5	0,7	0,4	6,4	5,2	5,3	8,7

Non-chloritized micas (biotite and muscovite), bioclast, organic matter, and heavy minerals occur as accessory constituents in the Agat Fm. Organic matter and bioclast have only been observed in small amounts (<0.5 %). Organic matter appears as black to brownish and elongated macerals that display a vascular structure. Bioclasts correspond to bivalve fragments and brachiopod shells. Finally, detrital phosphatic concretions and intraclasts are found in some samples forming massive aggregates of grains cemented by apatite (Fig. 6F). Its noteworthy that bioclasts, organic matter, and phosphatic concretions are widespread in conglomeratic facies (CPS and CFA), forming a few cm thick lenses (Fig. 3C, D).

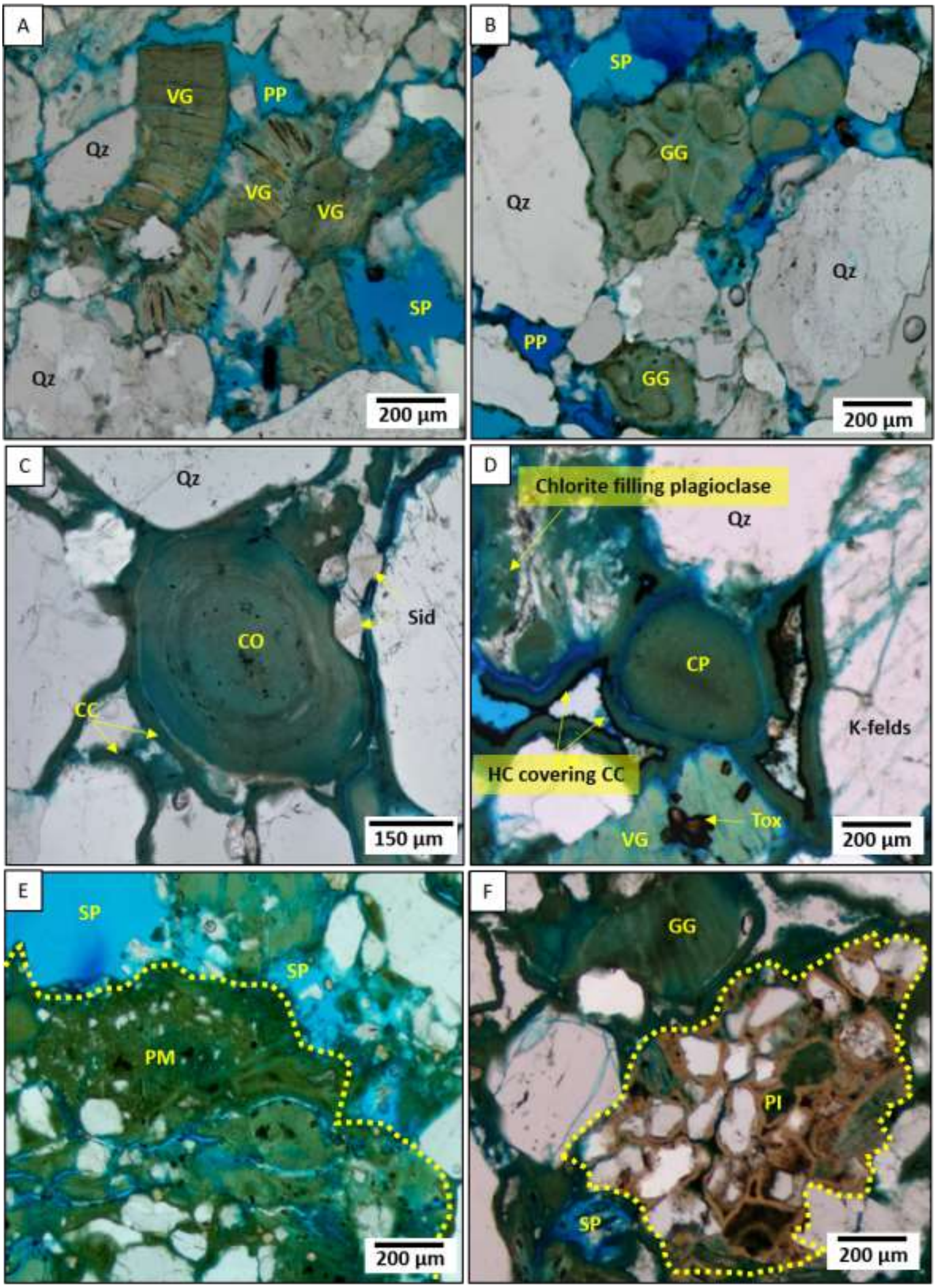

Fig. 6. Petrographic photomicrographs of the ductile grains in the Agat Fm: (A) Vermicular glauconite grains; (B) Globular glauconite grains; (C) Ooidal structure composed of chlorite; (D) Chlorite peloid showing massive structureless morphology associated with glauconite grain and thick chlorite coat, note that hydrocarbon is covering the chlorite coat in this sample; (E) Pseudomatrix highlighted by the yellow dashed line composed of chlorite and fine to very fine quartz grains; (F) Phosphatic intraclast highlighted by the yellow dashed line containing small size quartz and glauconite grains cemented by

apatite. (Qz: Quartz; K-felds: Alkali-feldspar; VG: Vermicular Glauconite; GG: Globular Glauconite; CO: Chlorite Ooid; CP: Chlorite Peloid; Tox: Titanium oxide; HC: Hydrocarbon; CC: Chlorite Coat; PM: Pseudo-Matrix, PI: Phosphatic Intraclast; PP: Primary Porosity; SP: Secondary porosity).

4.3. Texture and mineralogy of diagenetic minerals

Authigenic minerals consist of clay minerals (mainly chlorite), carbonate cement (calcite, siderite), and a small amount (<0.5%) of pyrite, apatite, secondary quartz, albite, and anatase.

4.3.1. Clay minerals

The clay mineralogy of the Agat Fm is composed of abundant chlorite, illite/mica, and minor Illite/Smectite (I/S) mixed layers.

Chlorite is the dominant pore-occluding cement in the Agat Fm. Chlorite is identified by the following d_{001} reflections 14.24 Å, 7.09 Å, 4.73 Å, and 3.54 Å. In both the UR and LR, the intensity of the even reflections (002 and 004) is higher compared to the odd reflections (001 and 003), suggesting iron-rich chlorite (Fig. 7A) (Brown and Brindley, 1980; Moore and Reynolds, 1997). Chlorite polytypes were determined from the random powder XRD analyses by identifying specific reflections (Bailey, 1988; Moore and Reynolds, 1997). Only the polytype Ib (ß= 90°) has been evidenced in the studied samples marked by the reflections at 2.69 Å, 2.65 Å, 2.51 Å, 2.34 Å, 2.15 Å, 1.96 Å (Fig. 7A). In addition, the d_{060} reflection of chlorite at 1.555 Å indicates trioctahedral chlorite.

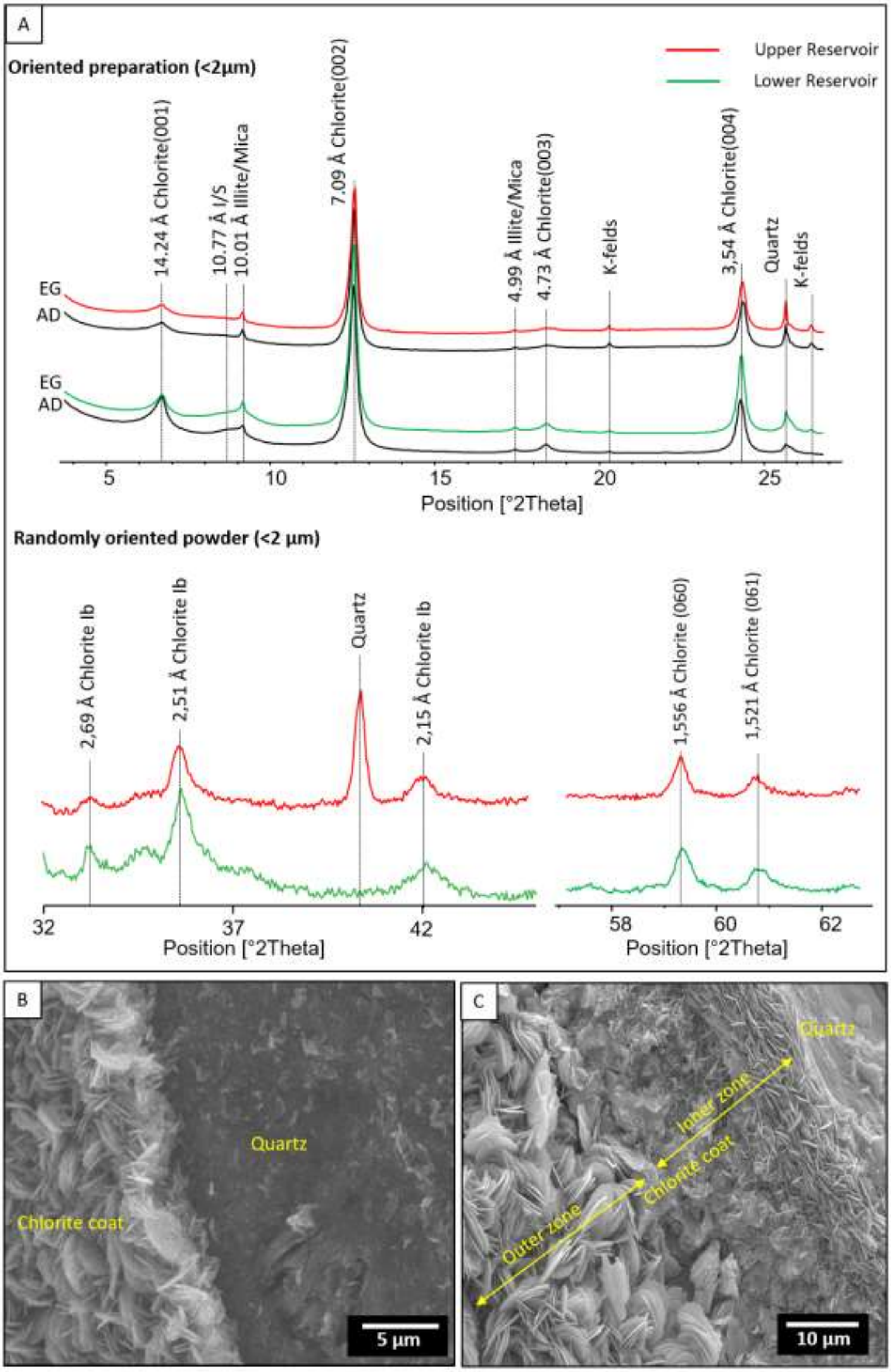
A
Oriented preparation (<2µm)
Upper Reservoir
Lower Reservoir
14.24 Å Chlorite(001)
10.77 Å I/S
10.01 Å Illite/Mica
7.09 Å Chlorite(002)
4.99 Å Illite/Mica
4.73 Å Chlorite(003)
K-felds
3,54 Å Chlorite(004)
Quartz
K-felds
EG
AD
EG
AD
5
10
15
20
25
Position [°2Theta]
Randomly oriented powder (<2 µm)
2,69 Å Chlorite Ib
2,51 Å Chlorite Ib
Quartz
2,15 Å Chlorite Ib
1,556 Å Chlorite (060)
1,521 Å Chlorite (061)
32
37
42
Position [°2Theta]
58
60
62
Position [°2Theta]
B
Quartz
Chlorite coat
5 µm
C
Quartz
Inner zone
Chlorite coat
Outer zone
10 µm

Fig. 7. (A) X-ray diffraction traces of oriented clay fraction specimens (<2 µm) along with X-ray diffraction traces of randomly oriented clay fractions (<2 µm) for some representative samples from the Upper Reservoir and the Lower Reservoir (AD: Air-dry, EG: Ethylene glycol-solvated); (C) SEM image of authigenic chlorite coat in the Upper Reservoir showing rosette-like morphology; (D) SEM image of chlorite coat in Lower Reservoir showing thick coating size and the presence of two zones.

SEM observations show that chlorites occur mainly as grain coats around detrital grains, ranging in size from 4 µm in the UR (Fig. 7B, 8A) and up to 30 µm thick in the LR (Fig. 7C, 8B). The latter is generally composed of two zones: an inner zone composed of small (av. 1.5 µm) randomly oriented chlorite grains and an outer zone composed of large (av. 4.5 µm) euhedral chlorite crystals oriented perpendicular to the grain surface (Fig. 7C, 8B). The outer zone engulfs small crystals of apatite, which seem to develop exclusively in the inner zone (Fig. 8B, C). Despite changes in morphology and texture, SEM-EDS analyses show no significant variation in the chemistry between the two zones (Table 2). Chlorite is also commonly found as a replacement of glauconitic grains forming ooidal structure (Fig. 8D) and as a replacement of lithic fragments forming a pseudo-matrix rich in mica (Fig. 8E). In rare cases, chlorite is associated with siderite in fractures and dissolution pockets in early calcite cement (Fig. 8F). Based on SEM-EDS analysis (Table 2), the composition of all the observed chlorites is very comparable, showing a chemical composition close to the chamosite endmember with an average Fe content of ~27 Wt %.

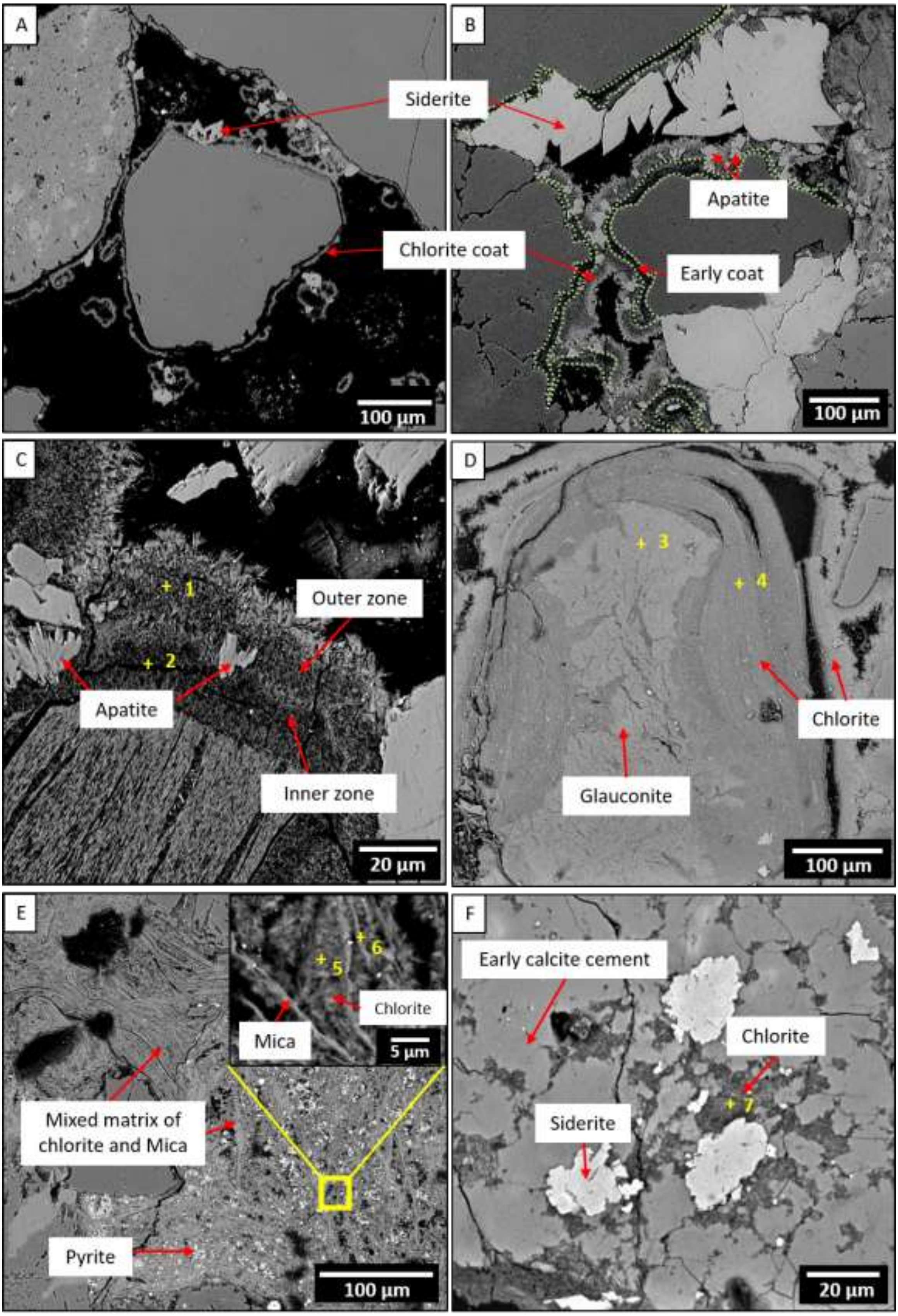

Fig. 8. SEM images showing the different forms of chlorite in the Agat Fm: (A) SEM micrograph of small siderite crystals associated with a thin chlorite coating size in a highly porous zone in the UR; (B) Authigenic chlorite, siderite, and apatite coating quartz grain in low porous zones in the LR, the green dotted line indicates the limit between early coat (inner zone) and the latter one (outer zone); (C)

Chlorite engulfing small apatite crystals which seems to develop exclusively on the inner zone of chlorite coat supporting a detrital origin for this zone; (D) Ooidal structure showing a nucleus composed of glauconite materials being replaced by chlorite; (E) Chlorite replacing mica materials in pseudomatrix; (F) Chlorite and siderite filling fractures and dissolution pockets within early calcite cement.

Illite/mica occurs as a minor component. The illite/mica is characterized by d_{001} reflections at 10.01 Å, 4.99 Å, and 3.33 Å. Most of this illite/mica is detrital and has a glauconite-like character based on petrographic observations. These grains show dissolution features and are being replaced by chlorite, as illustrated in Figure 8D, E. In addition to illite, the d_{001} reflection at 10.77 Å (air-dried conditions) suggests the presence of I/S mixed layer that shifted toward a lower 2 Theta angle after ethylene glycol saturation (Fig. 7A). This mixed layer is present in a small amount in the Agat Fm but increases relatively at the UR and LR boundary. The d_{001} reflection at 14.24 Å does not shift after ethylene glycol saturation, confirming the absence of any discrete smectite or chlorite/smectite mixed layers.

Table 2- Chemical composition of phases obtained by SEM-EDS analysis (the spot location is shown in a yellow cross in figure 8)

Weight (%)	1	2	3	4	5	6	7
	Chlorite	Chlorite	Glauconite	Chlorite	Chlorite	Mica	Chlorite
Si	15.6	13.0	21.1	17.2	15.0	20.8	12.8
Al	9.4	9.1	8.1	11.4	11.2	13.3	9.0
Fe	27.0	27.3	15.6	27.9	28.0	8.3	25.2
Mg	2.3	2.5	2.3	3.2	1.8	2.2	2.3
K	0.1	0.2	5.0	1.2	1.2	4.6	0.1

4.3.2. Carbonate cements

Calcite

Two generations of calcite cement were identified in the Agat Fm. The first generation (calcite 1) occurs only in two samples. It shows a sparry texture with a crystal size ranging from 20 µm up to 180 µm. Under cathodoluminescence, calcite 1 shows degraded texture with a dull orange luminescence (Fig. 9A). Calcite 1 occupies ~30 % of the intergranular volume and mainly occurs between loosely compacted grains showing floating texture. When placed in alizarin-potassium ferricyanide solution, calcite 1 shows a blue staining coloration, indicating an iron-rich composition (Lindholm and Finkelman, 1972). SEM observation also shows fracturing and pressure-solution (Fig. 9B). Fractures and secondary pores are filled with chlorite and siderite (Fig. 9B, C). The second generation (calcite 2) appears as a blocky to poikilotopic cement, with crystals reaching several millimeters in size. It shows uniformly bright orange luminescence with a very homogeneous texture (Fig. 9D). Unlike calcite 1, this generation occupies ~20 % of the intergranular volume of the samples and mainly develops between compacted grains filling the primary pore space. Calcite 2 is highly abundant at the boundary between the UR and LR, which considerably reduces porosity and permeability. However, it also occurs in varying proportions (1% up to 10%) at different depths in the reservoir. When placed in alizarin-potassium ferricyanide solution, all calcite cement shows a blue staining coloration indicating an iron-rich composition. In rare cases, calcite 2 appears to replace some dissolved plagioclase and lithic fragments (Fig. 9E). Remnants of calcite 2 (<0.5%) are found in many samples suggesting dissolution of this generation (Fig. 9F).

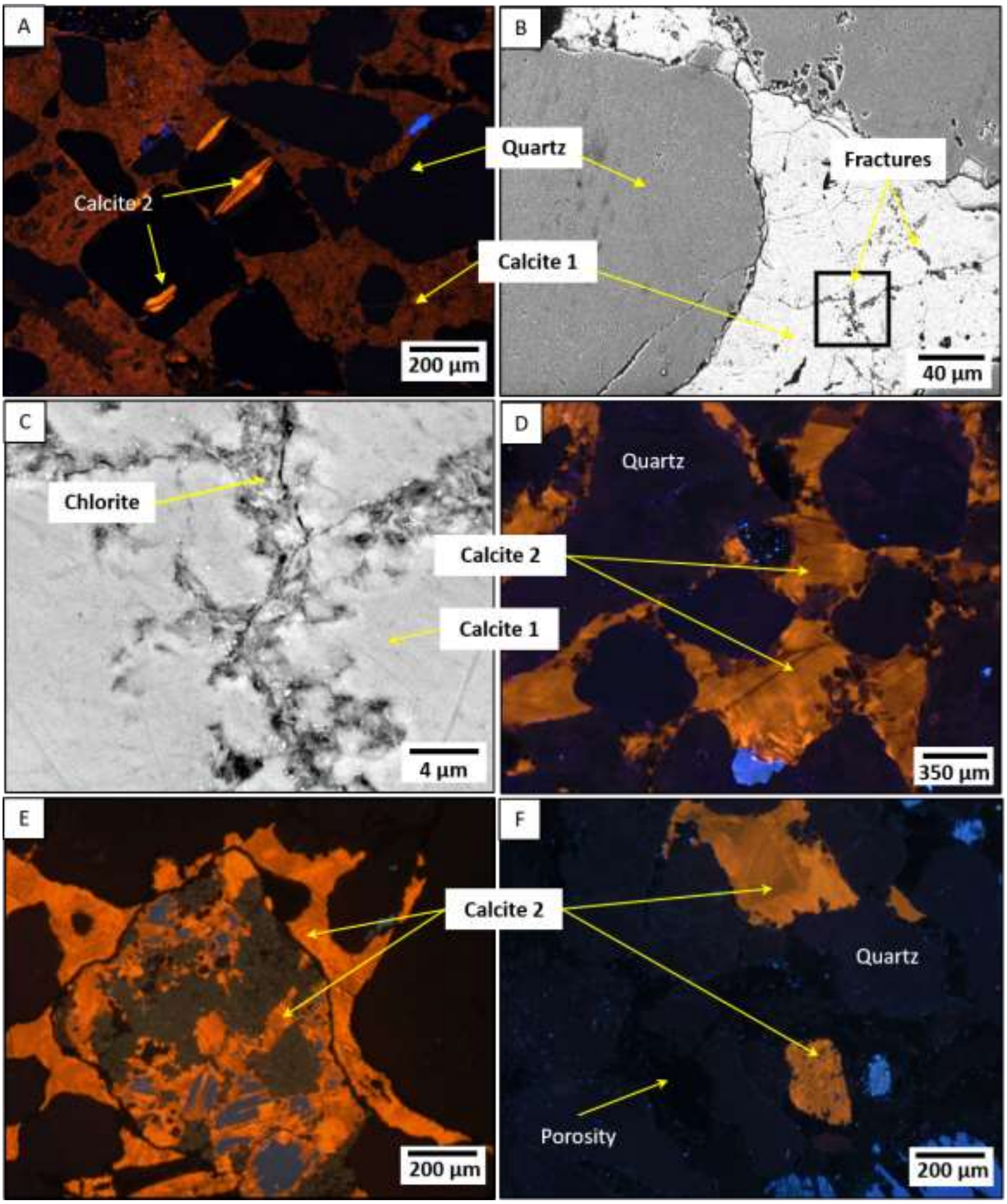

Fig. 9. (A) Cathodoluminescence photomicrograph showing the fine altered texture of blocky calcite 1, note that calcite 2 is also observed filling partially dissolved glauconite grains; (B) SEM micrograph of calcite 1 showing high intensity of stylolisation with the development of a fracture network; (C) Zoom on the black square in B showing fractures that are filled with chlorite; (D) cathodoluminescence photomicrograph showing the poikilotopic texture of the blocky calcite 2; (E) cathodoluminescence photomicrograph showing calcite 2 replacing plagioclase grains in lithic fragment; (F) Remnant of calcite 2 after dissolution.

Siderite

The average siderite amount in the studied samples is 1.5 %. However, this proportion increases at the boundary between the UR and LR, reaching 9 %. Also, siderite is highly concentrated in certain levels within the CPS facies, where they reach up to 15%, considerably reducing the porosity. The morphology of siderite varies significantly between the UR and the LR. In the UR, siderite forms small (<25 µm) rhombic-shaped crystals that are disseminated as coats around detrital grains (Fig. 8A), dissolved feldspar, and in the cleavage planes of glauconite grains. In the LR, siderite forms large crystals (>100 µm) that show radial extinction under polarized light with a rhombic edge (Fig. 8B). This increase in siderite size in the LR can lead, in some cases, to the total occlusion of pore space. Zonation is commonly observed in both the small and large siderite. Siderite crystals have a dark black core and a clear uncolored edge under the optical microscope (Fig. 10A).

4.4. Chemistry of carbonates

4.4.1. Elemental composition

The major and trace elements (Ca, Mg, Fe, Mn, and Sr) in calcite and siderite were measured by EPMA. For calcite 1, the Fe content varies from 2.51 to 3.32 Wt % (av. 2.95 Wt %), the Mg content varies from 0.14 to 0.21 Wt % (av. 0.18 Wt %) and those of Mn vary from 0.41 to 0.47 Wt % (av. 0.42 Wt %). The Sr content is below 0.1 Wt % (av.0.07 Wt %). For calcite 2, the Fe content varies from 0.58 to 1.76 Wt % (av. 1.21 Wt %), the Mn content varies from 0.16 to 0.49 Wt % (av. 0.34 Wt %), and the Mg content is less than 0.1 Wt %. The Sr content is relatively high, ranging from 0.25 to 0.38 Wt % (av. 0.31 wt. %). Overall, the Fe and Mg contents are higher in calcite 1, while the Ca and Sr contents are higher in calcite 2. Mn content is comparable in calcite 1 and 2. Unlike calcite, the chemical composition of siderite varies significantly from the core to the edges of the crystals. At least two stages of siderite growth can be distinguished based on elementary profiles and 2D maps of Fe, Mn, Mg, and Ca (Fig. 10B, C): an early-stage rich in Fe but poor in Ca, Mg, and Mn representing the core of siderite, and a later stage showing a strong decrease in Fe and an increase in Ca, Mg and Mn contents. In the core, the Fe contents vary from 44.0 to 46.0 Wt %, Mg varies from 0.33 to 1.51 Wt %, Ca varies from 1.31 to 1.85 Wt %, and Mn varies from 0.18 to 0.51 Wt %. On the edges, the Fe content varies from 39.1 to 41.9 Wt %, Mg varies from 1.77 to 2.34 Wt %, Ca varies from 2.72 to 3.37 Wt %, and Mn varies from 0.52 to 0.99 Wt %.

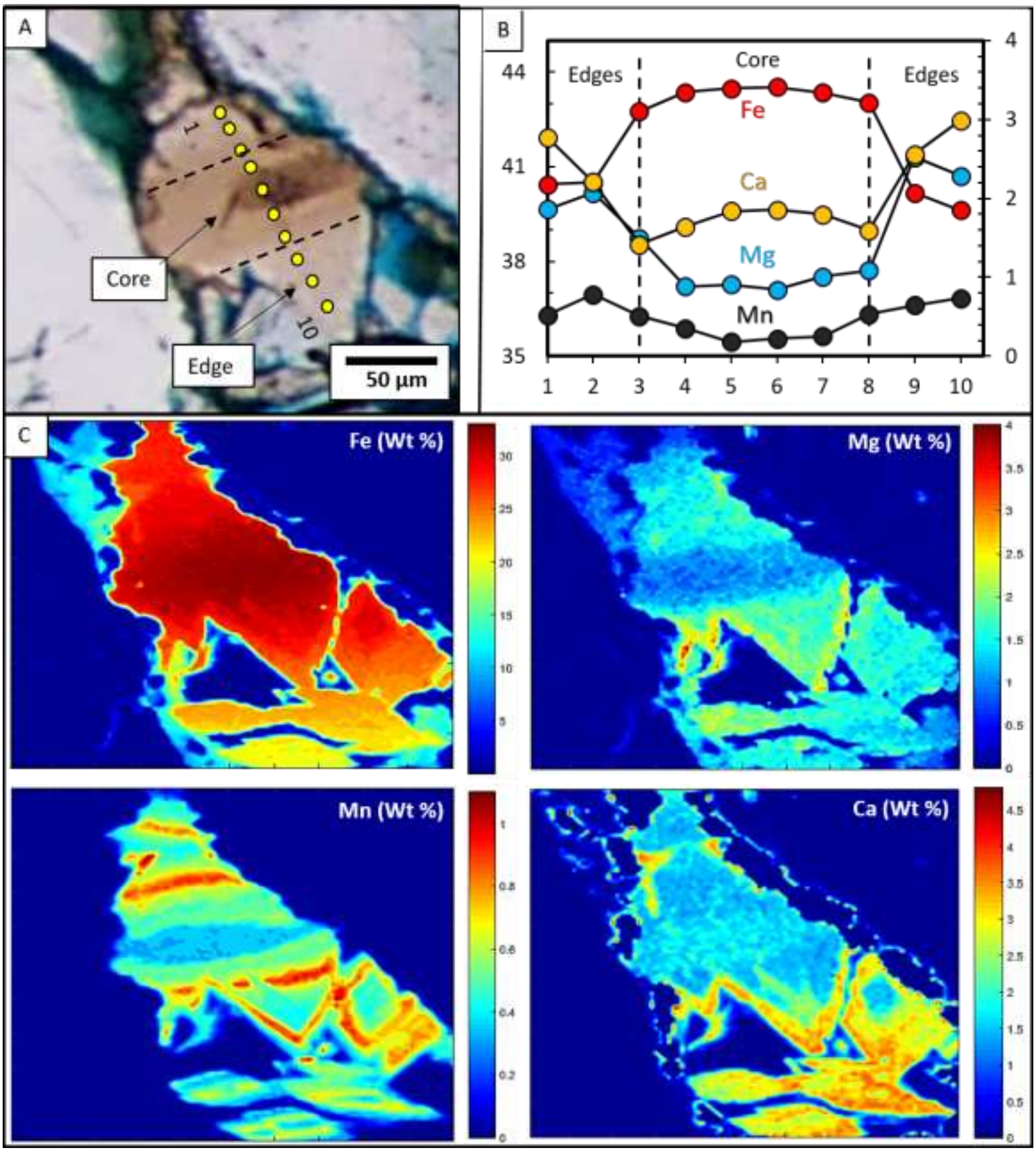

Fig. 10. (A) Microscope photograph of one of the analyzed siderites showing zonation, the locations of beam spots are represented by yellow dots; (B) Double y-axis plots presenting compositional changes in siderite along with WDS quantitative compositional profile, the left axis correspond to Fe Wt% and the right axis correspond to Ca, Mg, and Mn Wt%; (C) EPMA element distribution maps of Mn, Mg, and Ca for the analyzed siderite (Wt%: Weight %).

The REE concentration in carbonates was measured using LA-ICP-MS. Figure 11 shows the REE distribution in calcite and siderite together with the average bulk REE distribution of the Agat Fm and the marine carbonate from the Devonian Lennard Shelf reef complexes in Australia (Nothdurft et al., 2004). The mean total REE (ΣREE) in calcite 1 and 2 is 188 ppm and 65 ppm, respectively. Both calcite generations are characterized by a positive Ce anomaly (av. 1.79), a slightly positive Eu anomaly (av. 1.17), and depletion in all heavy REE (HREE). The shale-normalized REE distribution patterns in calcite cement are very different from marine carbonates but close to the average bulk chemistry of the Agat Fm. In the case of siderite, the spot size of the beam (~50 µm) is too large to sample the core and the edge of the crystal separately. The REE concentration in siderite is significantly lower (av. 9.8 ppm) than calcite 1 and 2 but exhibits a close distribution to the bulk rock of the Agat Fm showing a slightly positive cerium (av. 0.41) and europium anomalies (av. 1.16).

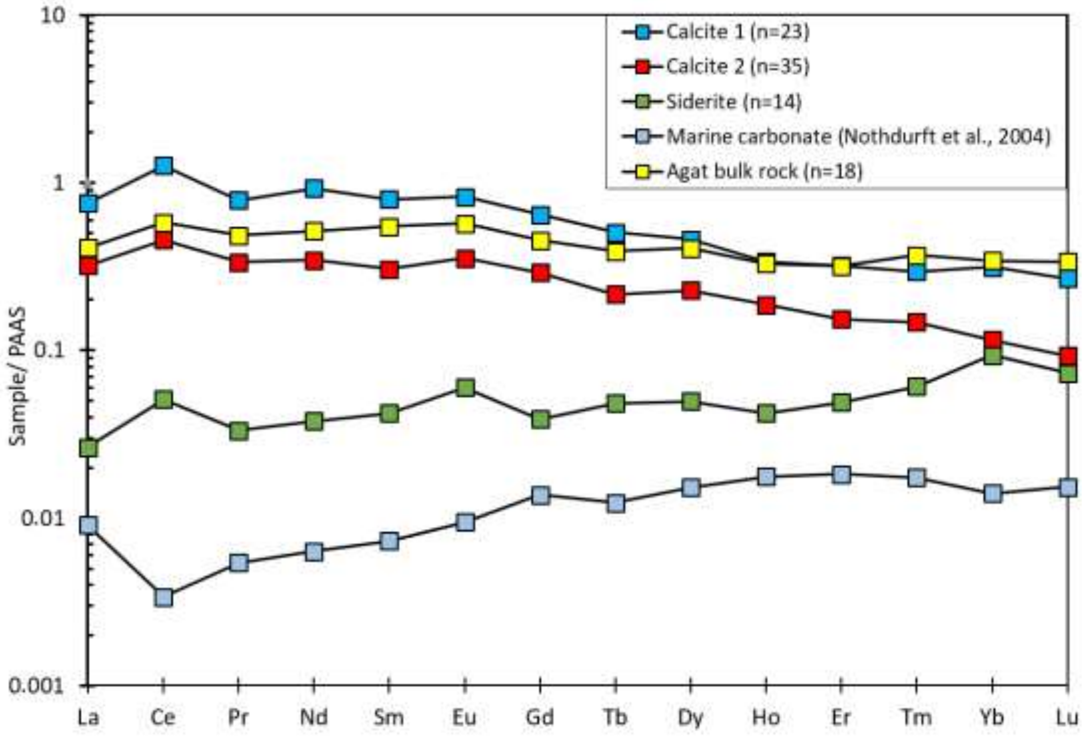

Fig. 11. PASS-normalized REE patterns for the average composition of calcite (1 and 2) and siderite compared to marine carbonate cement from the Devonian Lennard Shelf reef complexes (Nothdurft et al., 2004) and to the Agat bulk rock.

4.4.2. Carbon and oxygen stable isotope composition

The oxygen and carbon stable isotope composition in carbonates were measured using SIMS microanalysis. Oxygen isotopes show a strong contrast between calcite 1 and 2 (Fig. 12). The $\delta^{18}O$ values of calcite 1 range from –4.0 ‰ to –5.9 ‰ V-PDB with a mean value of −4.65 ‰ V-PDB (n=26). The $\delta^{18}O$ values of calcite 2 range from –8.2 to –11.5 ‰ V-PDB with a mean value of –10.8 ‰ V-PDB (n=32). The mean $\delta^{13}C$ values are comparable between both calcite generation (−11.7 ‰ V-PDB in calcite 1 and –10.6 ‰ V-PDB in calcite 2). However, Calcite 2 has a broad range of $\delta^{13}C$ values ranging from –4.8 ‰ V-PDB to –16.6 ‰ V-PDB. The lowest $\delta^{13}C$ values are generally found in calcite 2 in the LR, forming local precipitation, while the highest values correspond to calcite 2 found at the boundary between the UR and the LR.

The C and O isotopic measurements of siderite show a strong variation of $\delta^{18}O$ and $\delta^{13}C$ values between the core and the edges of the crystals (Fig. 12). The mean $\delta^{18}O$ and $\delta^{13}C$ values in the core are –5.13 ‰ V-PDB and –28.9 ‰ V-PDB (n=4), respectively. The mean $\delta^{18}O$ and $\delta^{13}C$ values of the edges are –0.10 ‰ V-PDB and –8.64 ‰ V-PDB (n=25), respectively. Between the core and the edges, a transition zone was identified with mean $\delta^{18}O$ and $\delta^{13}C$ values of –0.4 ‰ V-PDB and –16.9‰ V-PDB (n=7), respectively.

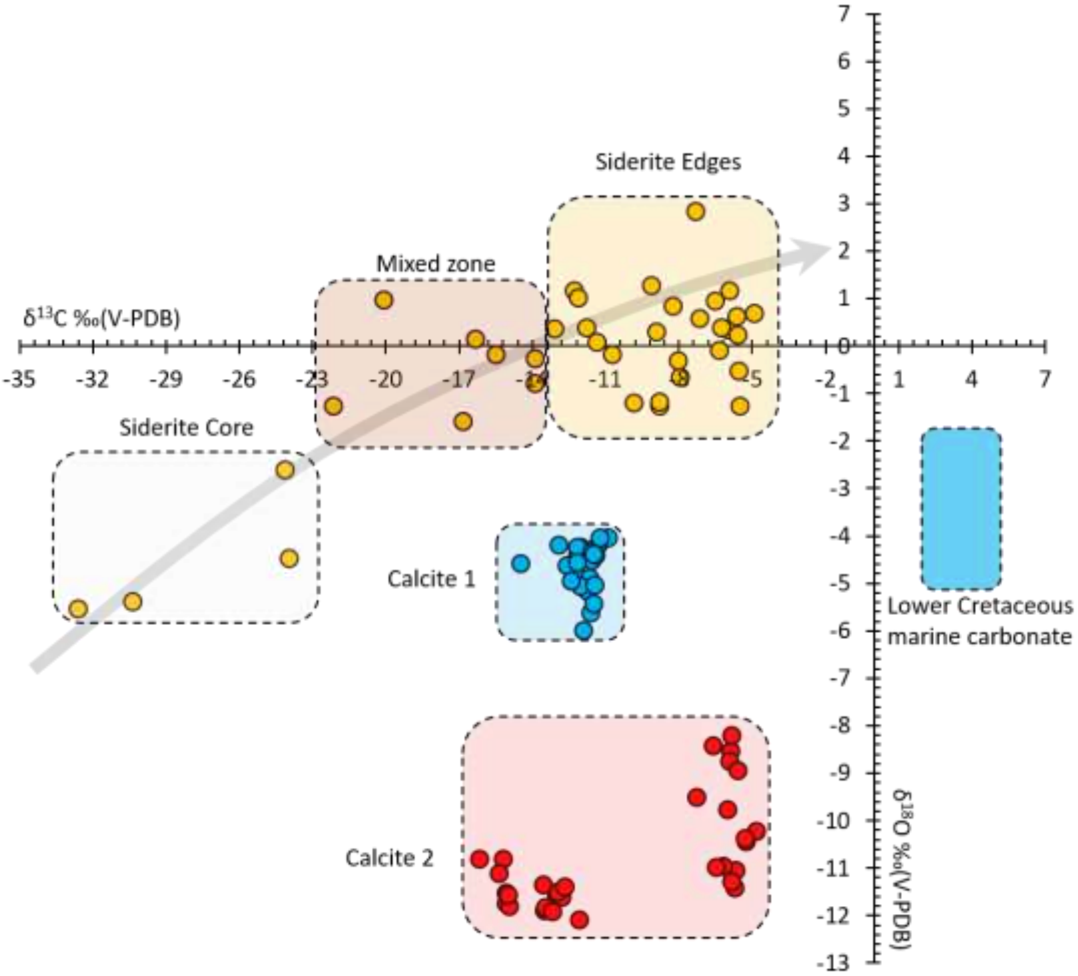

Fig. 12. Cross plot of the carbon versus oxygen isotopic signatures for various generations of calcite and siderite in the Agat Fm. The isotopic signature of typical Lower Cretaceous marine carbonates is from Allan and Wiggins (2019).

4.4.3. Fluid inclusion microthermometry in calcite 2 cement

Fluid inclusions are scarce in calcite 1 due to the small size of crystals and the strong fracturing. Therefore, the micro-thermometric analyses are focused on the calcite 2 cement, which has a more homogenous texture and bigger crystal sizes. Most fluid inclusions observed in calcite 2 are primary (aligned along with growth directions), single-phased (liquid water), elongated, or irregular in shape (Fig. 13A). Aqueous biphasic inclusions (liquid + vapor) are rare with tiny vapor bubbles. The inclusions show no hydrocarbon traces under ultraviolet light. Homogenization temperatures (Th) are between 85 °C and 105 °C, with a mean value of

93.4 °C (n=29, σ=4.4) (Fig. 13B). The final melting temperature (Tm) is between −1.4 °C and −3.4 °C, with a mean value ~~at~~ of −2.6°C, corresponding to the melting of ice. No other solid phases were observed. These final ice melting temperatures correspond to calculated salinity values between 2.4 and 5.5 Wt % NaCl with a mean value ~~at~~ of 4.3 Wt % NaCl (n=8, σ=1.25) (Bodnar, 1993). As previously mentioned, due to the very small size of the vapor bubbles, the final melting of ice was hardly visible in the smallest inclusions. The measured Th of calcite 2 corresponds to the minimum temperature at which fluid inclusions were entrapped. However, a pressure correction must be applied in order to determine the trapping temperature (Tt) of fluid inclusions, which also corresponds to the crystal growth temperature in the absence of post-trapping deformation (Goldstein and Reynolds, 1994). The pressure correction requires an estimation of the fluid trapping pressure. The Lower Cretaceous in the study area is generally under a hydrostatic pressure regime (hydrostatic gradient of 100 bar/km) (Riis and Wolff, 2020). By assuming a geothermal gradient of 35 °C/km (Baig et al., 2019) and a trapping pressure interval between 200 and 250 bar, the trapping temperature of fluid inclusions is ~105 ± 2 °C (Fig. 13C).

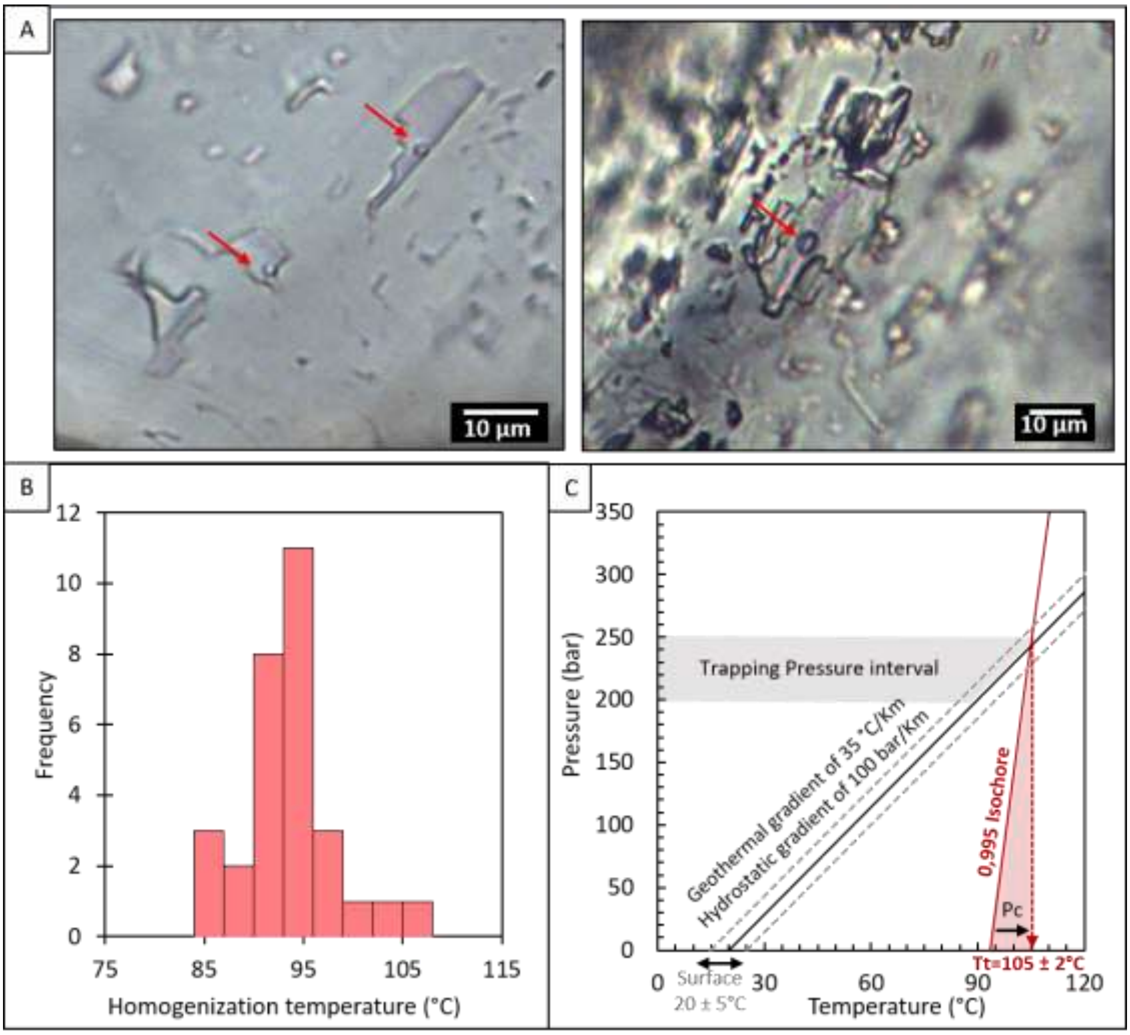

Fig. 13. (A) Microphotographs illustrating typical fluid inclusion types found in calcite 2 (the red arrows point to biphasic fluid inclusions); (B) Distribution of homogenization temperatures (Th) for fluid inclusions in calcite 2; (C) Pressure correction applied on fluid inclusions hosted in calcite 2 to calculate the trapping temperature (Tt). The isochore is obtained from fluid inclusion micro-thermometry (Steele-MacInnis et al., 2012).

4.5. Minor diagenetic minerals

In addition to the authigenic chlorite and carbonates, SEM observations reveal diagenetic pyrite, apatite, quartz, titanium dioxide (anatase), and albite present in small amounts (<0.5 %). Pyrite is mainly found as framboidal aggregates in some sedimentary lithic fragments and can also be found at the surface of detrital grains in association with chlorite (Fig. 14A). Apatite is present as an authigenic mineral forming acicular crystals between chlorite grains (Fig. 8B, C). EPMA results reveal a composition of fluorapatite with an average Wt % of P_2O_5, F, and CaO of 38.27 %, 6.9 %, and 55.5 %, respectively. Quartz cement is a minor component in the Agat

Fm and was only seen in some specific samples, where chlorite coats are detached or absent (Fig. 14A, B). The oxygen stable isotope composition in quartz overgrowth was measured using in situ SIMS microanalysis. The $\delta^{18}O$ values of quartz range from 22.5 ‰ to 29.6 ‰ V-SMOW, showing a strong mode at 26.8 ‰ V-SMOW (n=42). The average $\delta^{18}O$ value of quartz overgrowth is very consistent between the UR and the LR (av. 26.7 ‰ V-SMOW and 26.6 ‰ V-SMOW, respectively). By contrast, $\delta^{18}O$ values in the detrital quartz grains are very low compared to the overgrowth, showing an average of 11.2 ‰ V-SMOW (n=5). Anatase is observed as euhedral crystals, developing mainly on iron-rich grains like glauconite minerals (Fig. 14C). Finally, diagenetic albite (<0.5 %) is observed as tiny euhedral crystals with sharp edges partially replacing some dissolved K-feldspar grains (Fig. 14D). Under SEM, euhedral albite crystals develop in parallel to the cleavage plane of the parent K-feldspar grain. EDS analysis shows that albite has pure composition, reflecting a diagenetic origin (Chowdhury and Noble, 1993; Saigal et al., 1988).

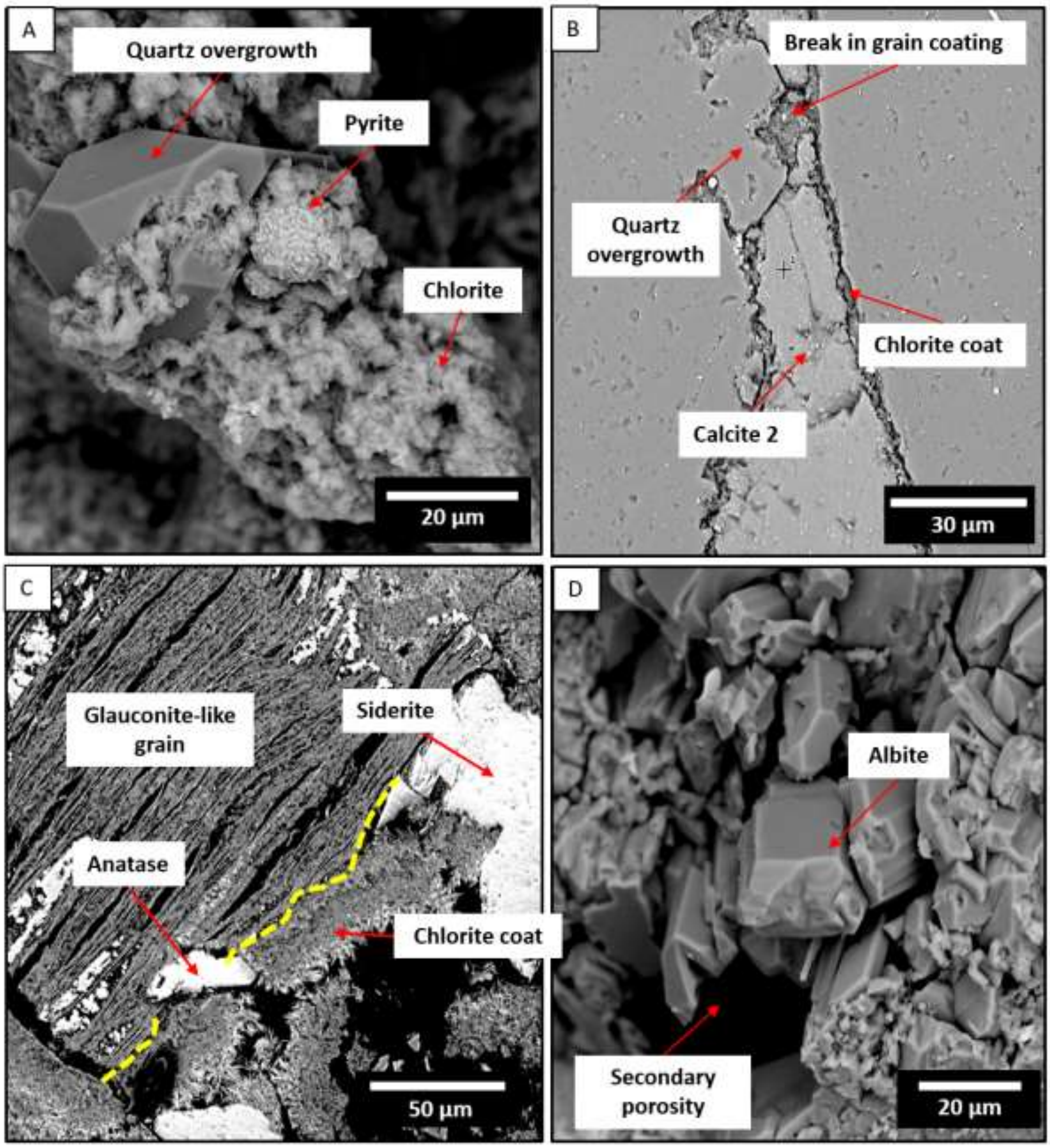

Fig. 14. SEM images of some accessory diagenetic minerals: (A) Framboidal pyrite associated with chlorite coat. Note the presence of euhedral quartz overgrowth developing where chlorite coat is absent; (B) Quartz overgrowth developing where chlorite coats are absent or detached. Calcite 2 postdates both quartz overgrowth and chlorite; (C) Anatase growing on glauconitic grain where chlorite coat is absent or detached (the yellow dashed line marks the limit between the chlorite coat and the grain); (D) Diagenetic albite showing euhedral crystals developing within the leached k-feldspar grain.

4.6. Porosity description

The porosity and permeability measurements show a contrasted reservoir quality between the UR and the LR (Fig. 15). In the UR, macroporosity, measured by point counting, varies from 10 % to 25 %. The primary porosity (av. 12.8 %) consists of small to large inter-granular pores that can reach more than 300 µm in size. Secondary porosity (av. 5.8 %) consists of moderate to large, oversized, and moldic pores that can reach several millimeters in size. Secondary porosity relates mainly to the dissolution of K-feldspar grains and locally calcite cement. Overall, the connectivity of the pore network varies from moderate to very good. Very good connectivity is found in samples that have well-developed secondary porosity (>7 %), a small number of ductile grains (<7 %), and a thin chlorite coat (<4 µm) (Fig. 15). This corresponds to samples that are located at the top of UR 2 (Fig. 15, Type I). Moderate connectivity is found in samples that show an increase in the amount of chlorite and ductile grains (>10 %) (Fig. 15). This corresponds to samples that are located at the base of UR 2 (Fig. 15, Type II). Also, some samples in UR 1 show low to moderate connectivity due to the presence of abundant ductile lithic fragments (Fig. 15, Type IV). The base of UR is cemented by calcite 2, showing permeability of less than 0.1 mD and macroporosity of less than 1 % (Fig. 15, Type VI). The porosity in this interval consists mainly of isolated secondary pores. Microporosity in the UR was estimated from the difference between helium porosity (total porosity) and point-counted porosity (macroporosity). The average microporosity in the UR is 8.5 % and is likely related to micropores in the clays (mainly chlorite) and ductile grains.

In the LR, macroporosity ranges from 1.3 % to 9 %. Primary porosity in the LR (av. 1.8 %) consists mainly of small inter-granular pores with a size smaller than 250 µm. The secondary porosity (av. 3.7 %) consists of moderate to large, oversized pores corresponding to the dissolution of K-feldspar grains. Overall, the connectivity of the pores network is generally weak and locally moderate. This is mainly due to the presence of a thick chlorite coat (>15 µm) and ~~to~~ the presence of abundant ductile grains (>15 %), which form a pseudo-matrix (Fig. 15, Type III). In addition, calcite and siderite are common in some levels in the LR, causing further reduction of primary porosity and connectivity of pores (Fig. 15, Type V, VI). The average microporosity in the LR is 18.6 %. The substantial increase in microporosity in the LR is mainly due to the large amount of chlorite and ductile grains.

In both reservoirs, some residual calcite 2 is present (<1%), suggesting that calcite had also undergone dissolution (Fig. 9F). However, its amount was difficult to estimate since calcite can dissolve completely without leaving diagnostic textures.

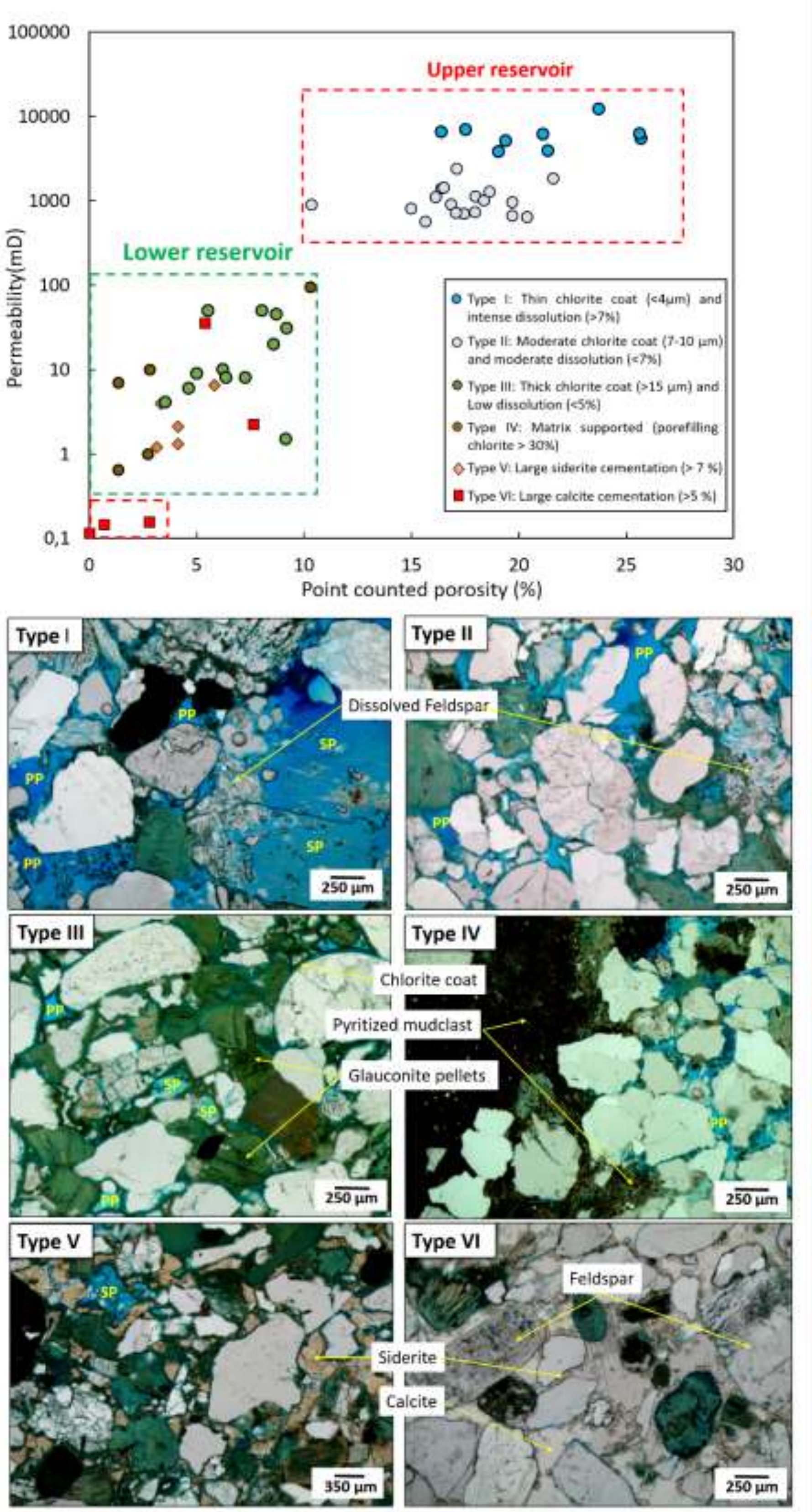

Fig. 15. Cross plot of permeability versus ~~measured~~ point counted porosity showing the effect of diagenesis on the reservoir quality. Petrographic microphotographs illustrate the pore network of the main rock types in the Agat Fm (PP: primary porosity, SP: secondary porosity).

5. Discussion

5.1. Paragenetic sequence

A paragenetic sequence is constructed based on textural relationships between the different authigenic phases (Fig. 16). The diagenetic evolution is represented along with the burial history of the Agat Fm reconstructed after Baig (2019). Three main stages of diagenetic evolution can be recognized in the Agat Fm:

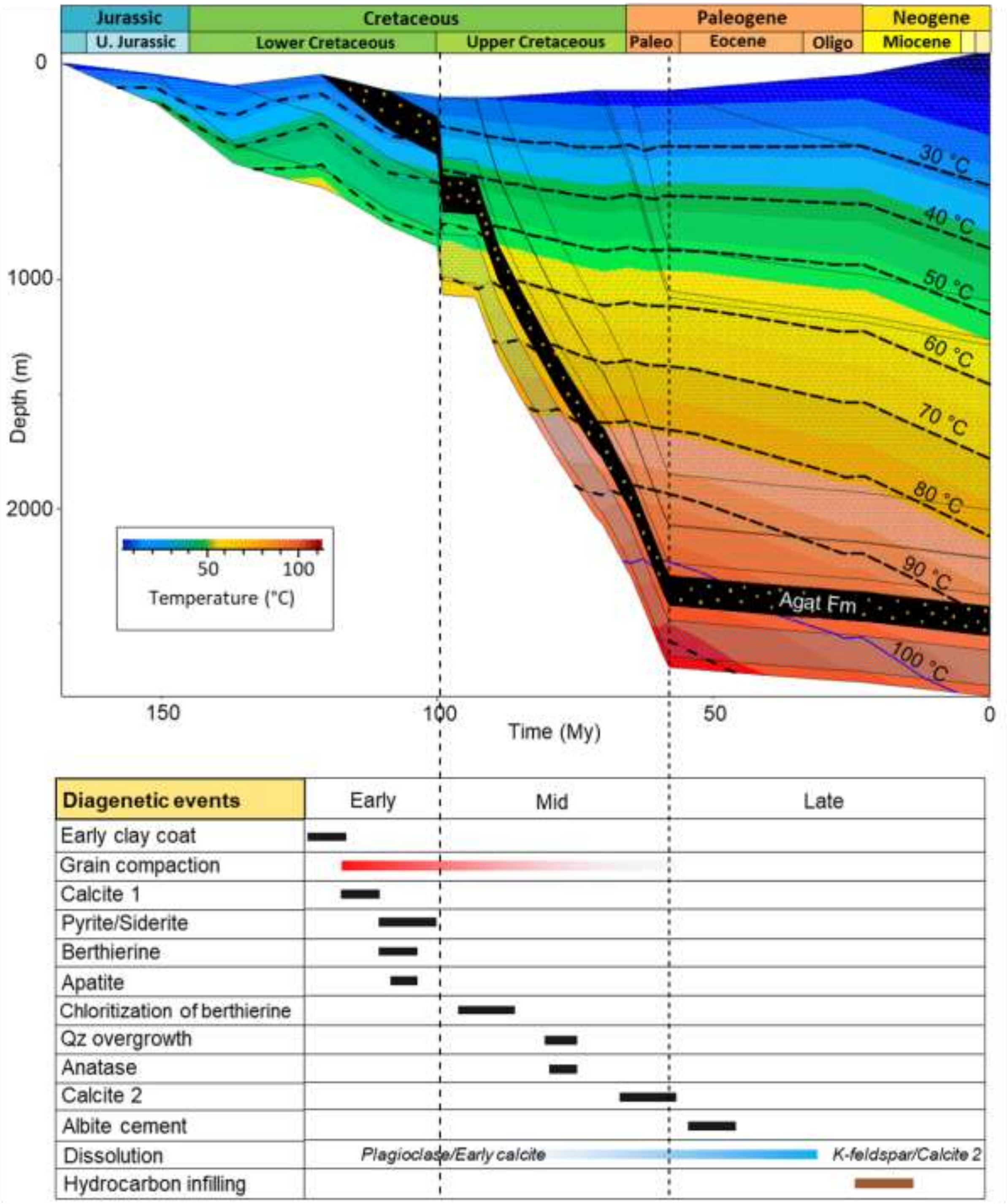

Fig. 16. Burial history and paragenetic sequence of the major diagenetic events in the Agat Fm.

5.1.1. Early diagenesis

Early diagenesis was initiated by the compaction and reorganization of detrital grains. As burial increases, the ductile framework is compressed and reworked, forming a pseudo-matrix. The latter is well developed in the LR due to the abundance of ductile grains and lithic fragments. However, the absence of sutured and concavo-convex contacts between the rigid framework grains indicates a limited pressure solution activity. The presence of some relics of early detrital coat, which correspond to the inner zone in chlorite coat, was probably inherited from shallow marine environments or related to the redistribution of the clay matrix in response to pore fluid movement during dewatering (Hansen et al., 2021). The compaction phase was interrupted by the precipitation of calcite 1 at certain levels of the reservoir. The high intergranular volumes of calcite 1 (30%) compared to calcite 2 (20%), and the loosely packed grains (Fig. 9A), suggest that calcite 1 develops before significant compactional porosity loss could occur. Furthermore, calcite 1 is locally dissolved and filled with chlorite, siderite, and apatite, which postdate calcite 1 (Fig. 9B, C).

The presence of chlorite in conjunction with siderite and minor framboidal pyrite suggests growth in a reducing environment at an early stage of burial (Curtis and Spears, 1968). These minerals are strongly associated with Fe-grains such as glauconite, Fe-ooids, and ferromagnesian lithic fragments which indicates that these grains are the main source of iron. Early siderite and pyrite are not coated by chlorite, suggesting that chlorite mainly replaces an early clay precursor. Also, authigenic apatite cement mainly develops on the inner zone of the chlorite coat (Fig. 9C), indicating that a clay precursor was present around detrital grains shortly after deposition. Many studies have found that chlorite and phosphate minerals like apatite are correlated in sandstone (Ehrenberg et al., 1998; Gould et al., 2010; Pe-Piper and Weir-Murphy, 2008). Pe-Piper and Weir-Murphy (2008) proposed that the abundance of phosphorus in sandstone reservoirs could indicate suitable diagenetic conditions for the precipitation of berthierine. The presence of apatite in the studied samples could be, therefore, an indicator of the presence of an early berthierine precursor.

5.1.2. Middle diagenesis

The onset of the middle diagenesis is characterized by the chloritization of the early clay precursor, probably berthierine, at a temperature greater than 50 °C (Beaufort et al., 2015). A small amount of quartz overgrowth is observed when chlorite coats are absent or detached, showing that chlorite has effectively inhibited quartz overgrowth (Fig. 14A, B). Similarly, anatase appears where chlorite coats are absent. Quartz overgrowth and anatase were followed by pervasive cementation of calcite 2, which encloses all the previous diagenetic minerals.

5.1.3. Late diagenesis

The late diagenesis is characterized by the intense dissolution of K-feldspar and locally calcite cement and by hydrocarbon emplacements. Dissolution of K-feldspar likely occurred during late diagenesis since most secondary pores are not filled with early diagenetic minerals such as siderite, chlorite, or late calcite cement. However, some grains of plagioclase are selectively leached before the dissolution of K-feldspar and are filled with chlorite and calcite 2 (Fig. 6D, 9E). The dissolution of K-feldspar was also associated with minor albite overgrowth, which fills some secondary pores. The final diagenetic event in the Agat Fm was the emplacement of hydrocarbons. This was evidenced by traces of bitumen covering chlorite coats in some samples (Fig. 6D). Also, the presence of only aqueous fluid inclusions in calcite 2 suggests that the hydrocarbon charge took place after calcite 2 cement.

5.2. Chlorite origin and formation mechanism

The formation of Fe-chlorite in low-temperature diagenetic systems is often the result of a solid-state transformation of an iron-rich clay precursor (Beaufort et al., 2015). The 7 Å, Fe-rich green serpentine-like clay minerals such as berthierine, odinite, and phyllite-V are the most common clay precursors for diagenetic Fe-rich chlorite (Virolle et al., 2022). These green clay minerals generally form in shallow marine settings (estuarine, deltaic, or inner shelf settings) under warm/tropical climate conditions (Ku and Walter, 2003; Odin, 1988). In sedimentary rocks, they occur as ooids, pre-compactional coatings, and matrix/pore filling (Odin, 1988). These minerals are metastable and tend to transform into chamosite (Fe-chlorite) upon burial (Beaufort et al., 2015; Delaloye and Odin, 1988; Hillier, 1994). The formation mechanism of chlorite in the Agat Fm can be divided into two main steps: (1) the first step occurs prior to the deposition in deep marine settings and involve the formation of an early clay precursor in shallow marine settings, (2) The second step occurs after deposition and involve the diagenetic transformation of the early clay precursor into continuous and well-crystallized chlorite coatings.

5.2.1. Synsedimentary deposition of early clay precursors in shallow marine settings

In the Agat Fm, the presence of abundant Fe-rich grains such as glauconite, ooids/peloids, ductile lithic fragments, and some relics of early detrital coats are all evidence of Fe-rich clay precursor for Fe-chlorite. The high concentration of glauconitic grains showing evidence of transport associated with some ooidal structures and phosphatic concretions indicates that these grains were derived from a shallow environment. In the North Sea, shallow marine sands are known to be potential chlorite factories particularly during the Jurassic and Cretaceous periods and therefore, could incorporate clay precursors in deep marine sands (Dowey et al., 2012; Ehrenberg, 1993; Griffiths et al., 2021). Various processes can explain the incorporation of clays within shallow marine sands: sediment mixing by bioturbation, mechanical infiltration of muddy waters, tidal pumping in coastal environments, and infiltration in the vadose zone in flood plains (Worden et al., 2020 and references therein). Estuaries and deltas are both suitable places for chlorite clay precursor development (Dowey et al., 2012). However, estuaries are generally more efficient than deltas in transporting sediments to deep water systems and are more suitable places for clay mineral accumulation and iron trapping in continental shelf areas (Daneshvar, 2011; Ehrenberg, 1993; Wetzel, 1993; Worden et al., 2020). Recent studies showed the importance of adhesive interactions between clay minerals and exoplymeric substances produced by diatoms acting as a glue in the formation of detrital clay coats in estuarine environments (Griffiths et al., 2019a, 2019b; Virolle et al., 2019; Wooldridge et al., 2017, 2019). The development of Fe-rich clay precursors in these settings also greatly depends on the source of sediments (type of bedrock) and fluvial activity, which is the main supply of Fe-materials and clays (Dowey et al., 2012). The recent study by Griffiths et al. (2021) shows that chlorite development and distribution can be strongly controlled by environmental conditions and fluvial influence. Chlorite mainly develops as pore-filling in tidal-fluvial channel sandstones deposited during high river discharge (flood events) or near river mouths leading to poor reservoir quality. By contrast, chlorite is found as a grain coating in sandstones with moderate fluvial influence, thus limiting quartz overgrowth and preserving porosity. The grain assemblages of the Agat Fm are remarkably similar to those described by Ehrenberg (1993) and Griffiths et al. (2021) from the Lower-Mid Jurassic shallow marine sandstone of the Norwegian continental shelf or by Virolle et al. (2022) from the Lower Cretaceous Wealden group of the Paris Basin. These periods coincide with the occurrence of many glauconitic and chamositic deposits in many sedimentary basins around the world (Van Houten and Purucker, 1984). Many authors have related this occurrence to an overall increase in the global temperature and the prevalence of warm and subtropical conditions similar to those of verdine facies in modern tropical waters (Delaloye and Odin, 1988; Dowey et al., 2012; Ehrenberg, 1993; Porrenga, 1967). Comparable paleo-environmental conditions may have prevailed during the deposition of the Agat Fm during the Aptian-Albian period, allowing the deposition of abundant Fe-grains/clays in some shelfal areas of Norway. These shallow marine sands were reworked during marine regression (lowstand) following the rejuvenation of older landmasses in the Norwegian North Sea and transported by turbidity currents forming slope fans (Brekke et al., 2001).

Despite similar mineralogy and diagenetic evolution between the UR and the LR, the Agat Fm shows a strong contrast in the relative abundance of iron-bearing minerals. Chlorite and Fe-grains are strongly concentrated in the LR compared to the UR. The latter shows an increase in the amount of quartz and feldspar. A likely scenario for this contrast could be related to changes in sediment supply or sediment provenance. The strong abundance of Fe-clays in the LR suggests that it was accumulated during a period when abundant Fe was delivered to the sea by the river systems. Conversely, the weak concentration of Fe-clays in the UR suggests that less Fe was delivered by the river systems. The source of Fe is likely to be derived from the alteration of lateritic soil profiles developing on Norway's mainland under warm, humid climates during the Aptian-Albian (Hay and Floegel, 2012; Larson, 1991; Lidmar-Bergström et al., 2009; Olesen et al., 2012). Lateritic profiles were probably thick and extensively developed during the deposition of the LR, providing a high amount of Fe and clays (Fig. 17A). The Fe supplied by river systems will subsequently be trapped near river mouths due to flocculation allowing a strong accumulation of Fe-clays (Dowey et al., 2012; Griffiths et al., 2021). During the deposition of the UR, the sediments were probably supplied from weakly altered rocks (parent bedrocks) when lateritic profiles were exhausted or weakly developed. This is consistent with the increase in k-feldspar and quartz in the UR relative to the LR, reflecting an increase in sediment supply from less weathered rocks (Fig. 17B).

It is noteworthy that environmental conditions occurring on the shelf may also have played an important role in the distribution of Fe-clays in the Agat Fm. Some samples in the LR contain abundant pore-filling chlorite due to the high abundance of Fe-grains and fine fraction materials filling primary intergranular pores. This, for example, is the case of samples found in conglomeratic facies (CPS) containing an important proportion of pore-filling chlorite (Table 1). These facies probably result from the reworking of shallow marine sands deposited under flood conditions or close to the estuarine turbidity maximum zone. This is comparable to what is observed in the Lower Jurassic Tilje Fm, where abundant pore-filling chlorite occurs during high fluvial activity or proximal to the central turbidity maximum zone (Griffiths et al., 2021). Estuarine turbidity maximum zones are suitable places for organic matter and trace metals flocculation, and therefore, they are hotspots for biological activity (Abascal-Zorrilla et al., 2020). This can explain why organic matters, bioclasts, and phosphatic concretions are mainly concentrated in conglomeratic facies while being absent from the rest of the Agat section. Samples with less porefilling chlorite are probably reworked from sediments deposited far from the central turbidity maximum or during periods of normal fluvial discharge (Griffiths et al., 2021).

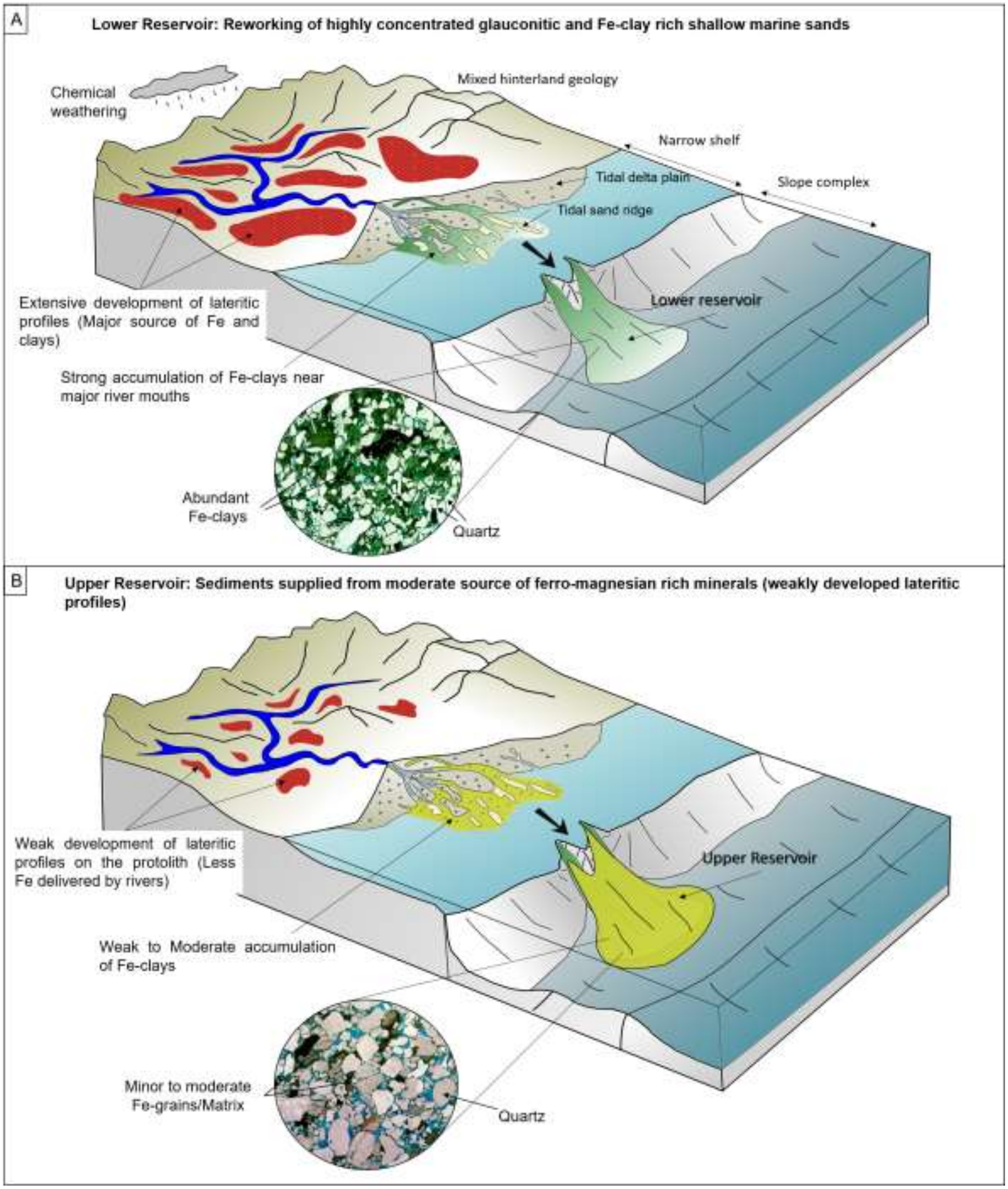

Fig. 17. Conceptual sedimentological model of the depositional environment of the study area. The Agat Fm is formed by the reworking of shallow marine sands in deep water. Shallow marine sands accumulate on a narrow shelf area during marine transgression. Remobilization occurs during regressive events following the rejuvenation of older landmasses in the Norwegian North Sea. (A) The LR is formed from the remobilization of concentrated glauconitic and Fe-clay-rich sands. Strong accumulation of Fe-clay occurs at the head of the estuary, where abundant iron is supplied by the fluvial system from extensively developed lateritic soil profiles. (B) The fluvial system delivers less Fe during the deposition of the UR (weak development of lateritic soils), leading to minor accumulation of Fe-clays.

5.2.2. Crystallization of Fe-chlorite

After deposition, the alteration of Fe-rich materials (grains/early detrital coats/lithic fragments) begins with the establishment of reducing conditions in the Agat Fm, leading to the formation of many Fe-minerals such as pyrite, siderite, and Fe-chlorite. However, the formation of Fe-chlorite at a low temperature requires the transformation from an intermediate clay precursor (Beaufort et al., 2015). This clay precursor is probably berthierine since all chlorites in the Agat sandstone are of Ib polytype (ß= 90°) (Beaufort et al., 2015; Billault et al., 2003; Hillier, 1994; Ryan and Hillier, 2002). Further evidence for a transformation from a berthierine precursor is also indicated by the 060 and 061 reflections of chlorite. The two peaks observed at 1.555 Å and 1.521 Å are consistent with those of berthierine (Virolle et al., 2022). The study of Virolle et al. (2022) of the Wealden Group sandstone of the Paris Basin documented the formation of berthierine at a depth between 0.8 km and 1 km and at a temperature of 35-40 °C. The growth of berthierine in the Agat Fm took place at an early stage of burial (<1 km) by replacing pre-existing Fe-rich materials like glauconite, ductile lithic fragments, and early detrital coat. With increasing burial (>1.5 km) and temperature (T>50 C°), Fe-chlorite will replace metastable berthierine through a solid-state transformation (SST) (Aagaard et al., 2000; Beaufort et al., 2015; Grigsby, 2001; Virolle et al., 2019). SST is a volume-conservative reaction resulting in similar shapes and sizes of the parental plates (Beaufort et al., 2015). The transformation of berthierine into chlorite is nearly complete at the present reservoir temperature (~89°C). The difference in the size of chlorite coating in the Agat Fm is mainly linked to the initial mineralogical composition of the sediments and the thickness of the inherited detrital coats. The LR contains almost twice the number of Fe-grains as the UR. Also, early coats are relatively thick in the LR. Consequently, this has led to a thick chlorite coat (>15 µm) in the LR, while being thinner in the UR.

5.3. Origin and formation mechanism of carbonate cement

5.3.1. Siderite and framboidal pyrite

Siderite and framboidal pyrite are among the earliest cement in the Agat Fm. Their close association with chlorite coat suggests growth under reducing conditions (Akinlotan, 2019; Curtis and Spears, 1968; Morad, 1998). The framboidal texture of pyrite is generally attributed to the biogenic formation by bacterial sulfate reduction (Folk, 2005). However, the pyrite amount is low compared to siderite, indicating a low concentration of Sulphur and, thus, weak development of the sulfate-reducing zone. Under such conditions, reduced iron will tend to form siderite and berthierine (Camprubí and Canet, 2009; Longstaffe, 2003; Taylor and Macquaker, 2011). Petrographic observations show zonation in siderite characterized by an overall decrease of iron concentration from the core to the edges (Fig. 10B, C). In addition, $\delta^{13}C$ and $\delta^{18}O$ values increase towards the edges (Fig. 12). Such zonation can be related to a change in the pore water chemistry due to bacterial activity (Wilkinson et al., 2000). Similar isotopic trends were observed by Bojanowski and Clarkson (2012) in siderite concretions from the Mississippian shales in Scotland, who attributed this trend to bacterial activity. The authors suggested that bicarbonate produced in the Sulfate-Reduction (SR) zone and in the Methanogenesis zone (Me) display contrasted $\delta^{13}C$ and $\delta^{18}O$ values. SR bacteria generally produce very low $\delta^{13}C$, while bacterial activity in the Me zone tends to produce higher $\delta^{13}C$ (Claypool and Kaplan, 1974; Irwin et al., 1977). Bojanowski and Clarkson (2012) also suggested that strong O isotope fractionation takes place when organic matter is oxidized via SR bacteria, which will eventually lead to ^{18}O-depleted bicarbonate. This model of siderite formation may explain the observed isotopic and chemical zonation. The presence of framboidal pyrite indicates that the sediments have experienced SR at some stage. In addition, the oxygen and carbon isotopic values are positively correlated, implying that they are both controlled by the same bacterial fractionation process. The core of siderite probably developed in the iron and SR zone, where a high amount of Fe is available, while the outer part probably grew in the Me zone with comparatively less available Fe. Using the oxygen fractionation equation of Zheng (1999) and by assuming that the $\delta^{18}O$ values of their parent fluid were close to Albian seawater (between −1.5 ‰ and +0.4 ‰ V-SMOW; Jaffrés, 2007), siderite precipitated at a temperature between 15 °C and 25 °C (Fig. 18A).

5.3.2. Calcite

Two generations of calcite cement were identified based on chemistry and texture. Calcite 1 precipitated at a shallow depth before significant compaction occurred. The REE distribution in calcite 1 is different from typical marine carbonate (Nothdurft et al., 2004) but is comparable with the Agat Fm bulk rock, suggesting that REE were sourced from local fluid-rock interactions. The positive Ce anomaly in calcite 1 could reflect such interaction of pore fluids with cerium-rich minerals such as phosphates, Fe-Mn oxyhydroxides, organic matter, and clay minerals (Abbott et al., 2019; Freslon et al., 2014; Girard, 2009; Hu et al., 2014; Tostevin et al., 2016). The slight positive Eu anomaly probably reflects a small contribution from plagioclase dissolution during burial (Lee et al., 2003). The measured $\delta^{18}O$ of calcite 1 suggests precipitation at a low temperature. By using the fractionation equation of Zheng (1999) and by assuming that the $\delta^{18}O$ values of their parent diagenetic fluids are between −4 ‰ V-SMOW (average value of present-day meteoric waters) and +0.4 ‰ V-SMOW (average value of Albian seawater (Jaffrés (2007)), the precipitation temperature is between 15 °C and 45 °C (Fig. 18B). The low carbon isotopic values of calcite 1 ($\delta^{13}C < -10$ ‰) could either be related to bacterial isotopic fractionation during the early burial or to carbon input from the thermal decarboxylation of organic matter (Girard, 2009; Jackson, 2012; Mansurbeg et al., 2009; Morad, 1998). The first hypothesis is more plausible since carbon derived from bacterial activity can display a wide range of δ^{13}C values (−25 ‰ to +16 ‰) (Clayton, 1994; Morad, 1998) and is more consistent with shallow precipitation depth. Pre-compactional calcite cement similar to calcite 1 was reported in many studies from North Sea reservoirs forming at a shallow depth (Bjorkum and Walderhaug, 1990; Saigal and Bjørlykke, 1987; Worden et al., 2019). Most of these studies proposed a possible origin for this early calcite to be the dissolution product of metastable phases such as aragonite and high Mg calcite. As there is no evidence of high Mg calcite residues in the Agat Fm, this assumption cannot be validated.

The second generation of calcite (Calcite 2) forms after quartz and chlorite, reflecting mesodiagenetic origin. Calcite crystallization during mesogenesis is very common in reservoirs from the Triassic, Jurassic, and Lower Cretaceous in the Norwegian North Sea (Kantorowicz et al., 1987; Mansurbeg et al., 2020; Morad et al., 1996; Saigal and Bjørlykke, 1987; Worden et al., 2019). The REE distribution of calcite 2 is identical to calcite 1 and to the Agat bulk rock, again indicating local fluid-rock interactions. Fluid inclusions in calcite 2 show Th values mostly between 85 °C and 105 °C, reflecting a deep burial origin. According to Baig et al. (2019) and Hansen et al. (2021), the Agat Fm in the studied well has reached a maximum burial depth of ~3,000 m which corresponds to a temperature of approximately 105 °C by assuming a geothermal gradient of 35 ℃/ km (Baig et al., 2019). This suggests that the precipitation of calcite 2 occurred near the maximum burial temperature. The salinity of fluid inclusions in calcite 2 (~4.3 Wt % NaCl eq.) is slightly higher than modern sea water (3.5 Wt % NaCl eq.) and consistent with the majority of formation waters in the Northern North Sea reservoirs showing a salinity less than 5 Wt % NaCl eq. (Bjørlykke and Gran, 1994). The measured δ^{18}O of calcite 2 and their approximate temperature of precipitation (90 °C - 105 °C) imply that the δ^{18}O values of their parent diagenetic fluids were approximately between +0.1 ‰ and +2.3 ‰ V-SMOW (av. +1.2 ‰ V-SMOW) (Fig. 18C). Positive δ^{18}O$_{water}$ could indicate evolved marine porewater due to interaction with silicate minerals during burial diagenesis (Denny et al., 2020). The δ^{13}C values of calcite 2 (−4.8 ‰ V-PDB to −16.6 ‰ V-PDB) indicate variable sources of dissolved carbon. The lowermost values (<−10 ‰) could be derived from the thermal decarboxylation of organic matter during late burial (Girard, 2009; Morad, 1998). Another source could be from the dissolution of early calcite 1 since they have similar δ^{13}C values. The upper most values (>−6 ‰) are likely derived from mixed sources, possibly with a contribution from marine carbonate or bioclast.

The calcium involved in the formation of late diagenetic calcite can have several potential sources. The most common in North Sea reservoirs is the dissolution and re-precipitation of marine-derived micrite, bioclasts, or early marine cement (Saigal and Bjørlykke, 1987; Worden et al., 2019). Other sources of calcium include the albitization of Ca-plagioclase (Schultz et al., 1989) and the dissolution of volcanoclastic detrital fragments (De Ros et al., 1997; Mtys, 2009). As both the shell fragments and plagioclase are scarce in the Agat Fm, they probably did not strongly contribute to the extensive calcite 2 cementation. It is, therefore, more likely that Ca was probably derived from the dissolution of early calcite cement such as Calcite 1.

5.4 Focus on quartz overgrowth

Quartz overgrowths are minor in the Agat Fm. They are only present where the chlorite coat is absent or detached. The scarcity of quartz overgrowth seems to be mainly related to the well continuous coverage of detrital grains by chlorite coat. Such continuous coverage suggests that the early clay precursor has survived transportation from the shelf to deep marine settings.

Several factors have probably favored the preservation of the early coating, including: (1) the narrow shelf during the Albian suggests that the sediments have only experienced short transportation distances, (2) the inner zone of chlorite coat varies from a few micrometers up to ~15 µm suggesting that the early clay coat was initially thick enough to be preserved during transport, (3) experimental studies by Verhagen et al. (2020) suggest that clay coat can withstand transportation by certain types of flows, and therefore could be exported and preserved in deep-marine environments. Furthermore, it is suggested that dewatering processes in high-density turbidites can significantly increase the grain coverage by detrital clay coats through the reorganization and elutriation of fine fraction materials (Porten et al., 2019). The combination of all these factors may have resulted in the well continuous coverage of grains by chlorite coats in the Agat Fm. Quartz overgrowth formed after the main phase of chloritization and prior to calcite 2. Their δ^{18}O values are identical in the UR and the LR, suggesting a single precipitation event. Assuming that the δ^{18}O values of their parent fluid were close to those of calcite 2, the precipitation temperature is between ~60 °C and ~85 °C (Fig. 18C). Such temperatures agree with the proposed paragenetic sequence (Fig. 16). The silica involved in the formation of quartz overgrowth can have several sources: (1) biogenic silica, (2) mineral reactions such as feldspar dissolution and clay mineral diagenesis, and (3) pressure solution of detrital quartz grains (Bjørlykke and Egeberg, 1993; Hyodo et al., 2014; Worden and Morad, 2000). In our case, biogenic silica is not observed. Also, feldspar dissolution probably did not significantly contribute to quartz overgrowth since it postdates most of the diagenetic events except for some minor plagioclase. Furthermore, the absence of sutured and concavo-convex contacts between detrital quartz grains indicates a limited pressure solution activity. Mu et al. (2015) suggested that the formation of berthierine in sandstone from the dissolution of glauconite is often associated with the release of silica and the development of quartz overgrowth. The formation of chlorite/berthierine and the dissolution and replacement of the pre-existing Fe-materials could be the source of silica in the Agat Fm.

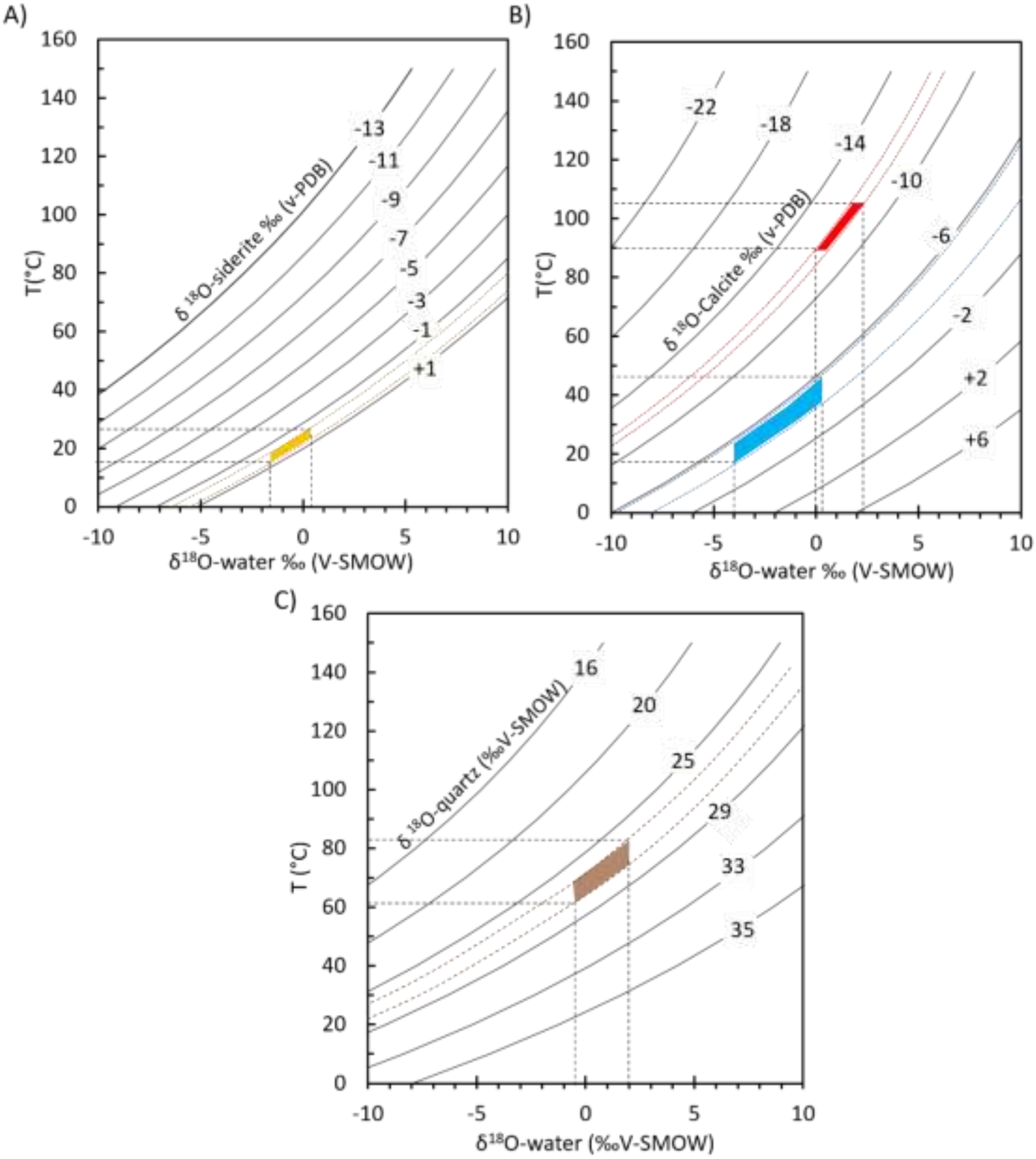

Fig. 18. (A) Oxygen isotope values of siderite plotted on the temperature-dependent, siderite-water oxygen fractionation curve of Zheng (1999); (B) Oxygen isotope values of various calcite generations (blue: calcite 1, red: calcite 2) plotted on the temperature-dependent, calcite-water oxygen fractionation curve of Zheng (1999). (C) Oxygen isotope values of quartz overgrowth plotted on the temperature-dependent, quartz-water oxygen fractionation curve of Zheng (1993).

5.5. Dissolution of K-feldspar and calcite

As previously mentioned, the major dissolution event in the Agat Fm took place during late diagenesis at a relatively high depth (>1500 m). This agrees with previous studies of North Sea sedimentary rocks that have also suggested that K-feldspar dissolution generally occurs during late diagenesis at depth >1500 m (Saigal et al., 1988; Wilkinson et al., 2001).

The dissolution of calcite cement and feldspar in sedimentary rocks depends on many parameters such as temperature, pH, pCO_2, salinity, porewater flow, and the presence of organic acids (Schmidt and Mcdonald, 1979; Zhang et al., 2009 and references therein). Many experimental studies have demonstrated that acidic pore waters favor the dissolution of feldspar and calcite (Helgeson et al., 1984; Matteo et al., 2018; Zhang et al., 2009). Some studies suggest that meteoric water can circulate deeply into the sediments and promote the dissolution reactions through the production of carbonic acids (Bjørlykke, 1983; Mansurbeg et al., 2012; Yuan et al., 2017). Other authors have proposed that organic acids produced by the maturation of sedimentary organic matter can increase the acidity of porewater and cause mineral dissolution (Schmidt and Mcdonald, 1979; Surdam et al., 1989; Yuan et al., 2015, 2019). Meteoric-water incursion usually happens during early diagenesis or telogenesis, when sediments are shallowly buried (<1500 m) (Mansurbeg et al., 2012, 2020). This mechanism is also generally associated with extensive dissolution and kaolinization of silicate grains. However, in the Agat Fm, the dissolution of k-feldspar occurs at considerable depth and the kaolinization is not observed. The second mechanism is, therefore, the most prominent. The presence of acidic fluids was noted above the pervasively calcite-cemented interval. The top of this interval is irregular and erosive, recording partial dissolution of calcite cement. A weak oil stain is generally found above and below this interval associated with the dissolution of calcite 2 and feldspar, showing that acidic fluids were mainly associated with hydrocarbon emplacement in the Agat Fm. It is also important to note that feldspar is not dissolved in the calcite-cemented interval (Fig.15), indicating that feldspars mainly dissolve after calcite 2 cementation. Organic acids likely entered the Agat Fm prior or during the installation of hydrocarbons (late diagenesis), causing the dissolution of feldspar and calcite, and releasing Al^{3+}, SiO_2, K^+, and Ca^{2+} in solution. However, the fate of these dissolution by-products is still unknown since most of the secondary pores are not filled with diagenetic precipitates, except for trace amounts of kaolinite, illite, and quartz cement. This can be explained by a mass transfer of the dissolution by-products from the leaching zone to a distant area. Such extensive dissolution in the Agat Fm probably occurred in relatively semi-open/open geochemical systems with high fluid fluxes, preventing supersaturation with respect to secondary minerals (Yuan et al., 2019).

5.6. Implications on the Agat reservoir quality

The porosity in the Agat Fm is controlled by mechanical compaction and by a series of cementation and dissolution events. The relative amount of porosity loss by compaction and cementation can be estimated by using the following equations of Lundegard (1992):

$$COPL = OP \frac{(100 - OP) * IGV}{(100 - IGV)} \quad (1)$$

$$CEPL = (OP - COPL) * \frac{CEM}{IGV} \quad (2)$$

Where COPL is the compaction porosity loss, CEPL is the cementation porosity loss, OP (%) is the original porosity before compaction estimated based on grain size and sorting using the chart of Beard and Weyl (1973), CEM (%) is the volume of cement, and IGV (%) is the inter-granular volume (total volume minus the volume percent of framework grain).

As shown in figure 19, compaction had a similar impact on the UR (av. COPL of 53 %) and the LR (av. COPL of 49 %). This compaction rate is consistent with the absence of sutured and concave-convex contacts, suggesting moderate overall compaction. However, the original porosity was much more reduced by cementation in the LR than in the UR. The CEPL is about 46 % in the LR and approximately 20 % in the UR. The increase in CEPL in the LR is mainly linked to the presence of abundant chlorite and locally carbonate cement. A detailed discussion of the influence of the major diagenetic mineral on the Agat reservoir quality is presented in the following sections.

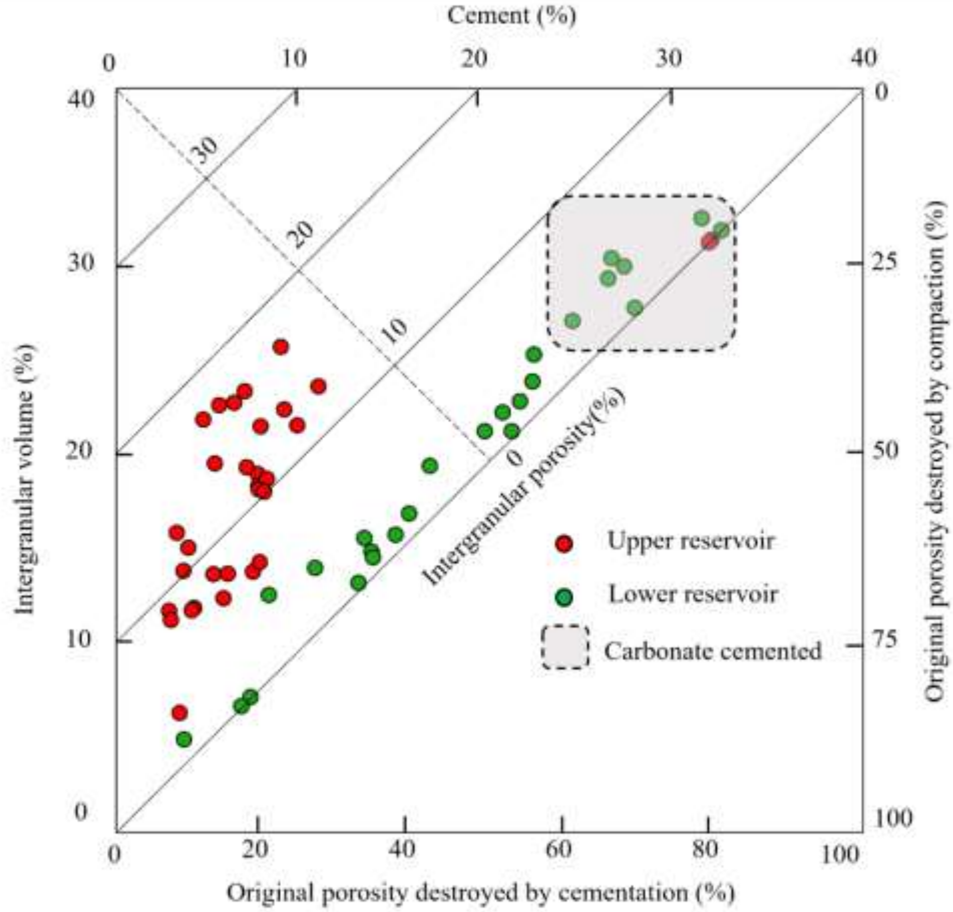

Fig. 19. Plot of intergranular volume (IGV) versus intergranular mineral cement (CEM) coded with reservoir division (diagram after Houseknecht, 1987).

5.6.1. Formation of Fe-chlorite coats

The effectiveness of chlorite in preserving porosity by inhibiting quartz overgrowth can be significantly balanced by the thickness of the chlorite coat and grain coat coverage. To prevent quartz overgrowth, detrital grains must be entirely coated since even a tiny gap can allow quartz crystals to grow (Bloch et al., 2002; Virolle et al., 2020; Worden et al., 2020). In addition, chlorite coat thickness should be thin to preserve the pore space. The thickness of the coat does not affect quartz overgrowth inhibition, as even a few micrometers of chlorite coats are enough to inhibit quartz cement (Worden et al., 2020). In the Agat Fm, most of the framework grains are entirely coated, and quartz overgrowth is rare. However, chlorite coat thickness has a significant impact on reservoir properties. The UR has better reservoir quality than the LR. High chlorite content in the LR is often associated with large coating thickness varying from 15 µm up to 30 µm. This, in turn, can occlude the pore throat and drastically reduce the connectivity of the pore network. Hence, the presence of chlorite in sandstone does not guarantee good reservoir quality: Sandstone with low to moderate chlorite content (2-5 %) and thin coating (~4 µm) is much better in preserving the pore space than those with high chlorite content (>10 %) and thick coating (>15 µm).

Besides reducing effective porosity, high chlorite content can affect the evaluation of oil saturation using resistivity logs by increasing the irreducible water saturation contained in chlorite microporosity (Anjos et al., 2009; Xia et al., 2020). In our case, microporosity reaches up to 50-60% of total porosity in the LR, while being less than 20% in the UR. This indicates that helium porosity does not necessarily reflect the effective porosity in chlorite-coated sandstone and that hydrocarbon estimations from resistivity logs in chlorite-bearing reservoirs can be significantly biased.

5.6.2. Carbonate cement

Carbonate cements (siderite and calcite) are heterogeneously distributed in the Agat Fm. Despite being less abundant than chlorite, their presence has locally led to the total occlusion of the pore space, causing reservoir segmentation. The ~3 m thick calcite-cemented interval at the boundary between the UR and LR shows the same mineralogy and texture as the overlying sandstone except for increased siderite content. Other calcite-cemented intervals of a few centimeters thick were also locally identified. The δ^{13}C values of calcite 2 in the main calcite-cemented interval are higher than those in the other disseminated occurrences, suggesting a contribution from ^{13}C-enriched carbonates like bioclast or marine carbonate. Small bioclast lenses are observed in the underlying conglomerate layer (CPS facies) (Fig. 2C), supporting therefore a bioclastic contribution. However, these lenses are only a few cm thick, which makes it difficult to confirm their role in the increase of the carbonate cementation at the boundary of the UR and the LR. Another possible interpretation for this interval would be the result of permeability variations between the UR and LR creating a localized fluid flow. When fluids move from a low permeability zone (i.e., LR) to a high permeability/underpressured zone (i.e., UR), the PCO_2 drops, promoting calcite precipitation (Morad, 1998). This interpretation predicts that the main calcite-cemented interval is continuous at the scale of the field. The investigations of seismic sections in the study area coupled with well logs of the nearest wells have revealed a strong discontinuity at the boundary between the UR and LR. Since this interval was not cored in other wells, the presence of extensive calcite cementation remains unknown.

The impact of siderite on reservoir properties is less important than calcite. However, the siderite proportion increases significantly at the boundary between the UR and LR and is locally high in the underlying CPS facies. The size of siderite crystals strongly increases at these levels, reaching up to 100 µm, causing a significant drop in permeability and porosity (Fig. 8B, 15).

This localized siderite cementation can be explained by an increase of the organically derived bicarbonate that will lead to preferential growth of siderite at the expense of Fe-clay minerals. Moreover, petrographic observations show that siderite preferentially nucleates on detrital grains that do not have early chlorite coats. In CPS facies, the framework grains are partially covered with an early detrital coat, providing more nucleation sites for siderite (Fig. 8B). Therefore, early chlorite coat precursors around framework grains inhibited siderite growth during early diagenesis, together with quartz overgrowth during late diagenesis (Pe-Piper and Piper, 2020).

5.6.3. Feldspar and calcite dissolution

The development of the secondary porosity has improved the quality of the Agat Fm, especially in the UR. Effective secondary porosity development is limited in the LR due to the weak connection of secondary pores which are often isolated by thick chlorite coatings. In contrast, in the UR, the presence of a high amount of dissolved feldspar has significantly increased the permeability (>1,500 mD). In some samples, the dissolution was so intense that the permeability reached values greater than 10,000 mD. This is the case at the top of the UR 2, representing a high dissolution zone of more than 15 m thick. The presence of this zone can be explained by a preferential fluid circulation favoring feldspar dissolution. Moreover, the top of the UR 2 contains a less proportion of ductile framework and chlorite (<4 %) compared to the base (>10 %). This has led to low sediment compaction, thus allowing fluids to circulate more easily.

In the case of calcite, the dissolution is evidenced in many samples but particularly from two meters above and below the calcite-cemented interval at the boundary between the UR and the LR. The former calcite cement was entirely dissolved at this level, leaving some residual calcite cement (0.5-1.5 %) (Fig. 9F) and some irregular pore textures. This suggests that the calcite-cemented interval at the boundary between the UR and the LR was thicker and has undergone dissolution at its top and base.

5.7. Conceptual diagenetic model and reservoir quality evolution of the Agat Fm

A conceptual diagenetic model of the main lithofacies in the Agat Fm is proposed in figure 20. The reservoir quality of the Agat Fm was controlled by several eogenetic and mesogenetic alterations mainly related to the initial mineralogy and depositional facies. The same diagenetic alterations were observed across the Agat Fm. However, the intensity of these alterations varies significantly between the UR and the LR. The LR was mainly affected by the development of a thick chlorite coating, which blocks the pore throats and increases the volume of ineffective porosity. Porosity and permeability were further reduced by the strong compaction of the ductile framework (Fe-grains and fine fraction materials), forming a pseudomatrix. On the contrary, such pseudomatrix is less developed in the UR, since it contains only a small amount of ductile framework. The presence of a thin chlorite coating has also retained more intergranular macropores in the UR. However, more pseudomatrix is found on top of the UR in hybrid bed facies (MLS), where abundant mudclasts can locally cause intense porosity loss upon compaction.

The distribution of carbonate cements was more localized compared to chlorite and pseudomatrix. Calcite cement mainly developed at the boundary between the UR and LR, forming a low permeability barrier. Such an extensively cemented zone is significant for reservoir evaluation since it can cause reservoir compartmentalization and lack of pressure communication between sand bodies. Similarly, strong siderite precipitation was associated with CPS facies. Organic matter and bioclastic fragments are widespread in these facies and have probably led to elevated aqueous HCO_3^-, promoting siderite growth instead of berthierine or chlorite. Early chlorite coating also partially covers sand grains in these facies, offering more nucleation sites for siderite.

The late dissolution of feldspars and calcite has significantly increased the reservoir quality in both the UR and the LR. Such dissolution probably took place in a relatively open/semi-open geological system with little precipitation of secondary minerals. The UR contains more feldspar than the LR and fluids can circulate more easily in the UR due to the high primary porosity. Therefore, mineral dissolution is widespread in the UR.

The detrital mineralogy plays the primary role in controlling the reservoir quality of the Agat Fm. The LR serves as an analog for glauconitic/chamositic rich sands, in which most of the intergranular porosity is blocked by chlorite coating and pseudomatrix. The UR provides an excellent case in which optimal chlorite growth conditions are present “chlorite Goldilocks zone” (Griffiths et al., 2021).

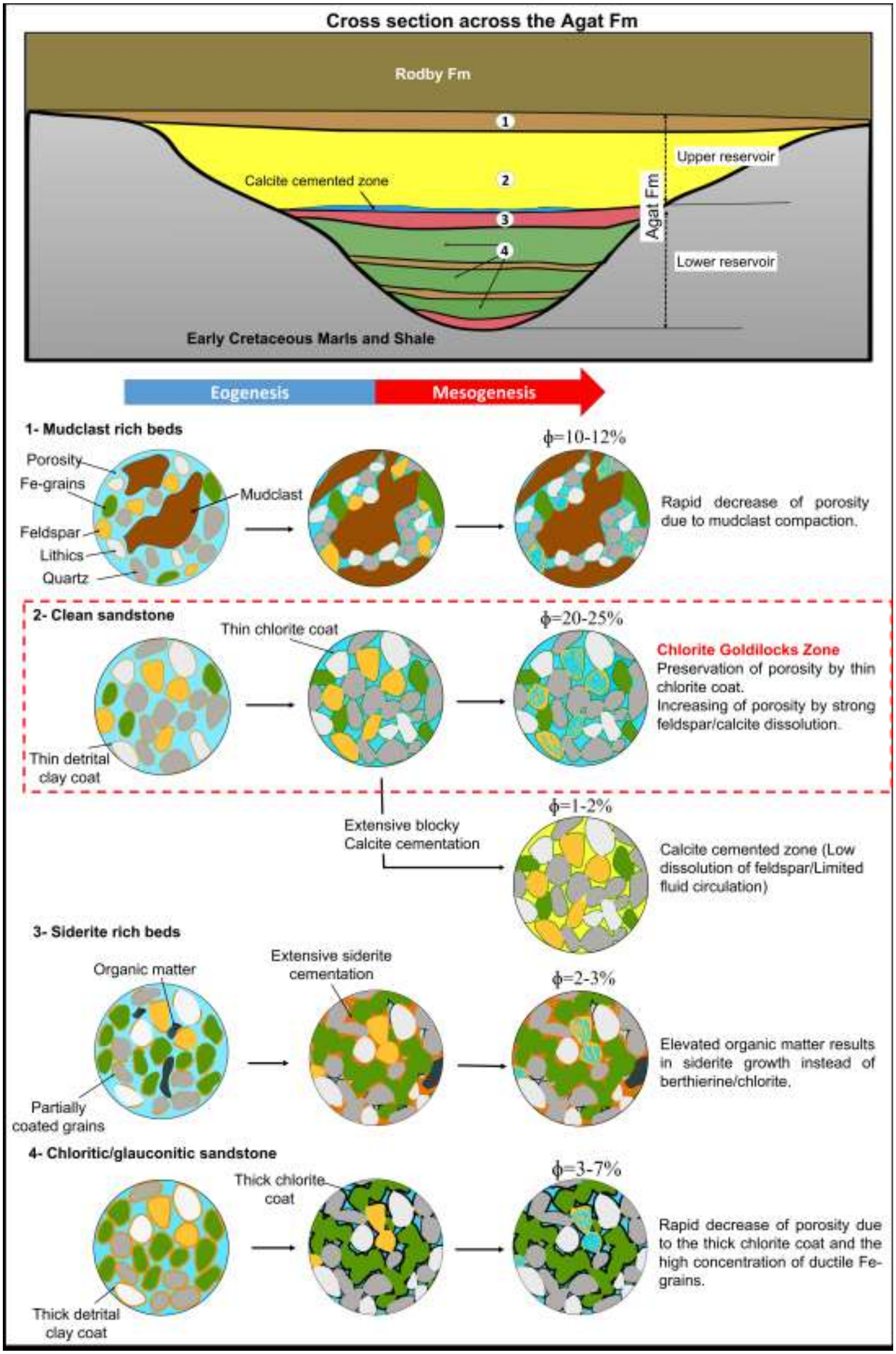

Fig. 20. Conceptual model of the diagenetic evolution pathways of the main lithofacies in the Agat Fm.

6. Conclusion

The reservoir quality of the Agat Fm has been controlled by a series of cementation, dissolution/recrystallization, and fluid flow events at different stages of burial. Several concluding remarks can be retained from this study, including:

- The Agat Fm was first subjected to highly reducing conditions during the early diagenesis, allowing chlorite, siderite, pyrite, and apatite crystallization. These minerals are highly concentrated in the lower part of the reservoir, where a thick chlorite coating (>15 µm) and large siderite crystals are developed. The significant increase in chlorite coating thickness drastically reduces the permeability of the lower part of the Agat Fm. In contrast, the chlorite coat is thinner in the upper part of the reservoir and has preserved permeability.
- The formation of chlorite coat has inhibited both quartz overgrowth and early siderite cement. Chlorite likely formed from a berthierine precursor that crystallized at low temperature (<40 °C) under reducing conditions.
- Bacterial activity during early diagenesis is evidenced through chemical and isotopic zonation in siderite crystals. Reactive Fe required for the crystallization of early berthierine, siderite, and pyrite is mainly sourced from the dissolution of Fe-rich detrital materials such as glauconite, ooids, lithic fragments, and detrital clay coats. These Fe-materials are highly concentrated in the lower part of the reservoirs causing excessive growth of berthierine/chlorite and, consequently a thick chlorite coating.
- The solid-state transformation of metastable berthierine into Fe-rich chlorite occurred with increasing burial and temperature (>50 °C). The formation of berthierine/chlorite was accompanied by minor quartz overgrowth at temperatures between 65°C and 85 °C.

- At higher temperatures (>85 °C), pores were plugged by the local precipitation of calcite, probably derived from the dissolution of an earlier calcite cement. Similar REE distribution in calcite generation, comparable to the bulk hosting rocks, suggests precipitation from local pore fluids instead of external fluids.
- Secondary pores formed through the dissolution of K-feldspar and calcite cement by pore waters enriched in acidic fluids prior to the hydrocarbon emplacement. This dissolution event has significantly enhanced the reservoir quality of the Agat Fm by creating a large macro-porosity and consequently increasing the permeability.

The Agat Fm offers an excellent example of how diagenesis influences the reservoir quality in turbidite sandstone. This work also highlights the role of initial detrital mineralogy in controlling the abundance and texture of chlorite coats in sandstone. Identifying the sources, transport, and accumulation conditions of Fe-rich detrital materials will help predict chlorite emplacements in similar geological settings worldwide.

Acknowledgments

This study was funded by Neptune Energy. The authors thank Neptune Energy Norge AS, PGNiG Upstream Norway AS, Idemitsu Petroleum Norge AS, and Sval Energi AS for access to samples, data, and information. The authors would also like to thank Serge Miska and Olivier Dufaure for assistance with XRD analysis and Julius Nouet for assistance with SEM. We are grateful to Philippe Blanc (Lithologie Bourgogne) for high-quality thin sections. The authors also thank Nourdine Bouden (CRPG) for assistance during the use of the SIMS Cameca 1280, and Nicolas Rividi and Michel Fialin (CAMPARIS, Sorbonne University) for their assistance during EPMA analytical sessions and Frédéric Haurine for assistance during ICM-PS analysis. Paris-Saclay University benefits from the Schlumberger Software Donation Program. We are grateful to Schlumberger for the PetroMod software license. We are also grateful to the reviewers (Joshua Griffiths, Guanhghui Yuan, and an anonymous reviewer) for their constructive comments and suggestions that improved this paper. We would also like to thank the associate editor Telm Bover-Arnal.

Appendixes

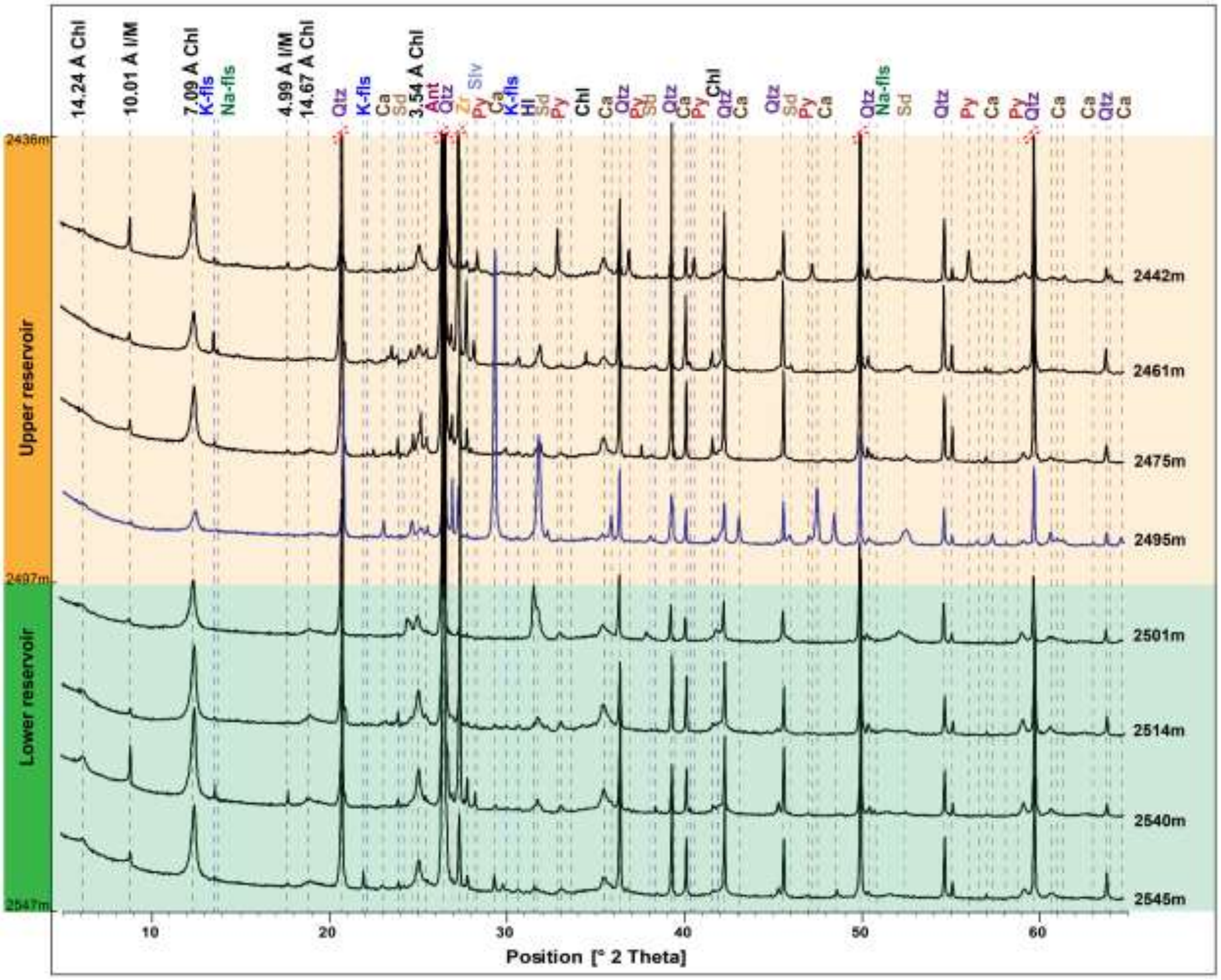

Figure A1. X-ray diffraction traces of some representative bulk powder samples from the UR and LR. Sample 308 in blue belongs to the calcite cemented interval. Chl = chlorite; I/M = illite/mica; Na-fs = Na-feldspar; Kfs = K-feldspar; Ant = anatase; Qtz = quartz; Ca = calcite; Py = pyrite; Sd = siderite; Zr = zircon; Hl = halite; Slv = sylvite.

References

Aagaard, P., Jahren, J.S., Harstad, A.O., Nilsen, O., Ramm, M., 2000. Formation of grain-coating chlorite in sandstones. Laboratory synthesized vs . natural occurrences . Clay Miner. 35, 261–269. https://doi.org/10.1180/000985500546639

Abascal-Zorrilla, N., Vantrepotte, V., Huybrechts, N., Ngoc, D.D., Anthony, E.J., Gardel, A., 2020. Dynamics of the Estuarine Turbidity Maximum Zone from Landsat-8 Data: The Case of the Maroni River Estuary, French Guiana. Remote Sens. 12. https://doi.org/10.3390/rs12132173

Abbate, E., Bortolotti, V., Passerini, P., 1970. Olistostromes and olistoliths. Sediment. Geol. 4, 521–557. https://doi.org/10.1016/0037-0738(70)90022-9

Abbott, A.N., Löhr, S., Trethewy, M., 2019. Are clay minerals the primary control on the oceanic rare earth element budget? Front. Mar. Sci. 6, 504. https://doi.org/10.3389/FMARS.2019.00504/BIBTEX

Ajdukiewicz, J.M., Larese, R.E., 2012. How clay grain coats inhibit quartz cement and preserve porosity in deeply buried sandstones: Observations and experiments. Am. Assoc. Pet. Geol. Bull. 96, 2091–2119. https://doi.org/10.1306/02211211075

Akinlotan, O., 2019. Sideritic ironstones as indicators of depositional environments in the Weald Basin (Early Cretaceous) SE England. Geol. Mag. 156, 533–546. https://doi.org/10.1017/S0016756817001017

Allan, J.R., Wiggins, W.D., 2019. Interpretation of Dolomites by Comparison to Marine Carbonates. Dolomite Reserv. Tech. Eval. Orig. Distrib. https://doi.org/10.1306/CE36576C6

Anjos, S.M.C., De Ros, L.F., Silva, C.M.A., 2009. Chlorite Authigenesis and Porosity Preservation in the Upper Cretaceous Marine Sandstones of the Santos Basin, Offshore Eastern Brazil. Clay Miner. Cem. Sandstones 289–316. https://doi.org/10.1002/9781444304336.ch13

Baig, I., Faleide, J.I., Mondol, N.H., Jahren, J., 2019. Burial and exhumation history controls on shale compaction and thermal maturity along the Norwegian North Sea basin margin areas. Mar. Pet. Geol. 104, 61–85. https://doi.org/10.1016/J.MARPETGEO.2019.03.010

Bailey, S.W., 1988. X-Ray Diffraction Identification of the Polytypes of Mica, Serpentine, and Chlorite. Clays Clay Miner. 1988 363 36, 193–213. https://doi.org/10.1346/CCMN.1988.0360301

Beard, D.C., Weyl, P.K., 1973. INFLUENCE OF TEXTURE ON POROSITY AND PERMEABILITY OF UNCONSOLIDATED SAND. Am. Assoc. Pet. Geol. Bull. https://doi.org/10.1306/819A4272-16C5-11D7-8645000102C1865D

Beaufort, D., Rigault, C., Billon, S., Billault, V., Inoue, A., Inoue, S., Patrier, P., 2015. Chlorite and chloritization processes through mixed-layer mineral series in low-temperature geological systems – a review. Clay Miner. 50, 497–523. https://doi.org/10.1180/claymin.2015.050.4.06

Billault, V., Beaufort, D., Baronnet, A., Lacharpagne, J.-C., 2003. A nanopetrographic and textural study of grain-coating chlorites in sandstone reservoirs. Clay Miner. 38, 315–328. https://doi.org/10.1180/0009855033830098

Bjorkum, P.A., Walderhaug, O., 1990. Lateral Extent of Calcite-cemented Zones in Shallow Marine Sandstones. North Sea oil gas Reserv. - II 331–336. https://doi.org/10.1007/978-94-009-0791-1_28

Bjorlykke, K., 1983. Diagenetic reactions in sandstones. Sediment Diagenes. 169–213. https://doi.org/10.1007/978-94-009-7259-9_3

Bjørlykke, K., Egeberg, P.K., 1993. Quartz Cementation in Sedimentary Basins. Am. Assoc. Pet. Geol. Bull. 77, 1538–1548. https://doi.org/10.1306/BDFF8EE8-1718-11D7-8645000102C1865D

Bjørlykke, K., Gran, K., 1994. Salinity variations in North Sea formation waters: implications for large-scale fluid movements. Mar. Pet. Geol. 11, 5–9. https://doi.org/10.1016/0264-8172(94)90003-5

Bloch, S., Lander, R.H., Bonnell, L., 2002. Anomalously high porosity and permeability in deeply buried sandstone reservoirs: Origin and predictability. Am. Assoc. Pet. Geol. Bull. 86, 301–328. https://doi.org/10.1306/61eedabc-173e-11d7-8645000102c1865d

Blott, S.J., Pye, K., 2001. GRADISTAT: a grain size distribution and statistics package for the analysis of unconsolidated sediments. Earth Surf. Process. Landforms 26, 1237–1248. https://doi.org/10.1002/ESP.261

Bodnar, R.J., 1993. Revised equation and table for determining the freezing point depression of H2O-Nacl solutions. Geochim. Cosmochim. Acta 57, 683–684. https://doi.org/10.1016/0016-7037(93)90378-A

Bojanowski, M.J., Clarkson, E.N.K., 2012. Origin of siderite concretions in microenvironments of methanogenesis developed in a sulfate reduction zone: An exception or a rule? J. Sediment. Res. 82, 585–598. https://doi.org/10.2110/jsr.2012.50

Brown, G., Brindley, G.W., 1980. X-ray Diffraction Procedures for Clay Mineral Identification. Cryst. Struct. Clay Miner. their X-Ray Identif. 305–360. https://doi.org/10.1180/MONO-5.5

Bugge, T., Tveiten, B., Bäckström, S., 2001. The depositional history of the cretaceous in the northeastern North Sea. Nor. Pet. Soc. Spec. Publ. 10, 279–291. https://doi.org/10.1016/S0928-8937(01)80018-7

Camprubí, A., Canet, C., 2009. "Berthierine and chamosite hydrothermal: Genetic guides in the Peña Colorada magnetite-bearing ore deposit, Mexico." Earth, Planets Sp. 61, 291–295. https://doi.org/10.1186/BF03352910

Chowdhury, A.H., Noble, J.P.A., 1993. Feldspar albitization and feldspar cementation in the Albert Formation reservoir sandstones, New Brunswick, Canada. Mar. Pet. Geol. https://doi.org/10.1016/0264-8172(93)90083-5

Claypool, G.E., Kaplan, I.R., 1974. The Origin and Distribution of Methane in Marine Sediments. Nat. Gases Mar. Sediments 99–139. https://doi.org/10.1007/978-1-4684-2757-8_8

Clayton, C.J., 1994. Microbial and Organic Processes. Quant. Diagenes. Recent Dev. Appl. to Reserv. Geol. 125–160. https://doi.org/10.1007/978-94-011-0189-9_4

Copestake, P., Sims, A.P., Crittenden, S., Hamar, G.P., Ineson, J.R., Rose, P.T., Tringham, M.E., 2003. Lower Cretaceous, in: Evans, D., Graham, C., Armour, A., Bathurst, P. (Eds.), The Millennium Atlas: Petroleum Geology of the Central and Northern North Sea. Geological Society of London, pp. 191–211.

Crittenden, S., Cole, J.M., Kirk, M.J., 1998. The distribution of Aptian sandstones in the central and northern North Sea (UK sector) - a lowstand systems tract play. Part 2: distribution and exploration strategy. J. Pet. Geol. 21, 187–211. https://doi.org/10.1111/j.1747-5457.1998.tb00653.x

Curtis, C.D., Spears, D.A., 1968. The formation of sedimentary iron minerals. Econ. Geol. https://doi.org/10.2113/gsecongeo.63.3.257

Daneshvar, E., 2011. Role of provenance on clay minerals and their distribution in modern estuaries.

De Ros, L.F., Morad, S., Al-Aasm, I.S., 1997. Diagenesis of siliciclastic and volcaniclastic sediments in the Cretaceous and Miocene sequences of the NW African margin (DSDP Leg 47 A, Site 397). Sediment. Geol. https://doi.org/10.1016/S0037-0738(97)00030-4

Delaloye, M.F., Odin, G.S., 1988. Chapter A1 Chamosite, The Green Marine Clay From Chamoson; A Study of Swiss Oolitic Ironstones. Dev. Sedimentol. 45, 7–28. https://doi.org/10.1016/S0070-4571(08)70056-6

Denny, A.C., Fall, A., Orland, I.J., Valley, J.W., Eichhubl, P., Laubach, S.E., 2020. A history of pore water oxygen isotope evolution in the cretaceous travis peak formation in East Texas. Bull. Geol. Soc. Am. 132, 1626–1638. https://doi.org/10.1130/B35291.1

Dowey, P.J., Hodgson, D.M., Worden, R.H., 2012. Pre-requisites, processes, and prediction of chlorite grain coatings in petroleum reservoirs: A review of subsurface examples. Mar. Pet. Geol. 32, 63–75. https://doi.org/10.1016/j.marpetgeo.2011.11.007

Ehrenberg, S.N., 1993. Preservation of anomalously high porosity in deeply buried sandstones by grain-coating chlorite: examples from the Norwegian continental shelf. Am. Assoc. Pet. Geol. Bull. 77, 1260–1286. https://doi.org/10.1306/f4c8e062-1712-11d7-8645000102c1865d

Ehrenberga, S.N., Dalland, A., Nadeau, P.H., Mearns, E.W., Amundsen, E.F., 1998. Origin of chlorite enrichment and neodymium isotopic anomalies in Haltenbanken sandstones. Mar. Pet. Geol. 15, 403–425. https://doi.org/10.1016/S0264-8172(98)00023-3

Estupiñan, J., Marfil, R., Delgado, A., Permanyer, A., 2007. The impact of carbonate cements on the reservoir quality in the Napo Fm sandstones (Cretaceous Oriente Basin, Ecuador). Geol. Acta 5, 89–107. https://doi.org/10.1344/105.000000312

Folk, R.L., 2005. Nannobacteria and the formation of framboidal pyrite: Textural evidence. J. Earth Syst. Sci. https://doi.org/10.1007/BF02702955

Folk, R.L., 1980. Petrology of sedimentary rocks. Hemphill publishing company.

Freslon, N., Bayon, G., Toucanne, S., Bermell, S., Bollinger, C., Chéron, S., Etoubleau, J., Germain, Y., Khripounoff, A., Ponzevera, E., Rouget, M.L., 2014. Rare earth elements and neodymium isotopes in sedimentary organic matter. Geochim. Cosmochim. Acta. https://doi.org/10.1016/j.gca.2014.05.016

Girard, J.-P., 2009. Carbonate Cementation in the Middle Jurassic Oseberg Reservoir Sandstone, Oseberg Field, Norway: A Case of Deep Burial–High Temperature Poikilotopic Calcite, in: Carbonate Cementation in Sandstones. https://doi.org/10.1002/9781444304893.ch13

Glennie, K.W., 2009. Petroleum geology of the north sea: Basic concepts and recent advances: Fourth edition, Petroleum Geology of the North Sea: Basic Concepts and Recent Advances: Fourth Edition. https://doi.org/10.1002/9781444313413

Goff, J.C., 1984. Hydrocarbon Generation and Migration from Jurassic Source Rocks in the East Shetland Basin and Viking Graben of the Northern North Sea. Pet. Geochemistry Basin Eval. https://doi.org/10.1306/M35439C16

Goldstein, R.H., Reynolds, T.J., 1994. Systematics of Fluid Inclusions in Diagenetic Minerals, Systematics of Fluid Inclusions in Diagenetic Minerals. SEPM (Society for Sedimentary Geology). https://doi.org/10.2110/scn.94.31

Gould, K., Pe-Piper, G., Piper, D.J.W., 2010. Relationship of diagenetic chlorite rims to depositional facies in Lower Cretaceous reservoir sandstones of the Scotian Basin. Sedimentology 57, 587–610. https://doi.org/10.1111/j.1365-3091.2009.01106.x

Gradstein, F.M., Waters, C.N., Charnock, M., Munsterman, D., Hollerbach, M., Brunstad, H., Hammer, Ø., Vergara, L., 2016. Stratigraphic guide to the cromer knoll, shetland and chalk groups, north sea and norwegian sea. Newsletters Stratigr. 49, 73–280. https://doi.org/10.1127/nos/2016/0071

Griffiths, J., Worden, R.H., Utley, J.E.P., Brostrøm, C., Martinius, A.W., Lawan, A.Y., Al-Hajri, A.I., 2021. Origin and distribution of grain-coating and pore-filling chlorite in deltaic sandstones for reservoir quality assessment. Mar. Pet. Geol. 134, 105326. https://doi.org/10.1016/j.marpetgeo.2021.105326

Griffiths, J., Worden, R.H., Wooldridge, L.J., Utley, J.E.P., Duller, R.A., 2019a. Compositional variation in modern estuarine sands: Predicting major controls on sandstone reservoir quality. Am. Assoc. Pet. Geol. Bull. 103, 797–833. https://doi.org/10.1306/09181818025

Griffiths, J., Worden, R.H., Wooldridge, L.J., Utley, J.E.P., Duller, R.A., Edge, R.L., 2019b. Estuarine clay mineral distribution: Modern analogue for ancient sandstone reservoir quality prediction. Sedimentology 66, 2011–2047. https://doi.org/https://doi.org/10.1111/sed.12571

Grigsby, J.D., 2001. Origin and Growth Mechanism of Authigenic Chlorite in Sandstones of the Lower Vicksburg Formation, South Texas. J. Sediment. Res. 71, 27–36. https://doi.org/10.1306/060100710027

Hansen, H.N., Løvstad, K., Lageat, G., Clerc, S., Jahren, J., 2021. Chlorite coating patterns and reservoir quality in deep marine depositional systems – Example from the Cretaceous Agat Formation, Northern North Sea, Norway. Basin Res. 33, 2725–2744. https://doi.org/https://doi.org/10.1111/bre.12581

Haq, B.U., 2014. Cretaceous eustasy revisited. Glob. Planet. Change. https://doi.org/10.1016/j.gloplacha.2013.12.007

Hay, W.W., Floegel, S., 2012. New thoughts about the Cretaceous climate and oceans. Earth-Science Rev. 115, 262–272. https://doi.org/10.1016/j.earscirev.2012.09.008

Helgeson, H.C., Murphy, W.M., Aagaard, P., 1984. Thermodynamic and kinetic constraints on reaction rates among minerals and aqueous solutions. II. Rate constants, effective surface area, and the hydrolysis of feldspar. Geochim. Cosmochim. Acta. https://doi.org/10.1016/0016-7037(84)90294-1

Hendry, J.P., Trewin, N.H., Fallick, A.E., 1996. Low-Mg calcite marine cement in Cretaceous turbidites: Origin, spatial distribution and relationship to seawater chemistry.

Sedimentology. https://doi.org/10.1111/j.1365-3091.1996.tb01508.x

Hillier, S., 1994. Pore-lining chlorites in siliciclastic reservoir sandstones: electron microprobe, SEM and XRD data, and implications for their origin. Clay Miner. 29, 665–679. https://doi.org/10.1180/claymin.1994.029.4.20

Houseknecht, D.W., 1987. Assessing the Relative Importance of Compaction Processes and Cementation to Reduction of Porosity in Sandstones. Am. Assoc. Pet. Geol. Bull. 71, 633–642. https://doi.org/10.1306/9488787F-1704-11D7-8645000102C1865D

Houseknecht, D.W., Ross, L.M., 1992. Clay Minerals in Atokan Deep-Water Sandstone Facies, Arkoma Basin: Origins and Influence on Diagenesis and Reservoir Quality. Orig. Diagenesis, Petrophysics Clay Miner. Sandstones 227–240. https://doi.org/10.2110/pec.92.47.0227

Hu, Y., Feng, D., Peckmann, J., Roberts, H.H., Chen, D., 2014. New insights into cerium anomalies and mechanisms of trace metal enrichment in authigenic carbonate from hydrocarbon seeps. Chem. Geol. https://doi.org/10.1016/j.chemgeo.2014.05.014

Hyodo, A., Kozdon, R., Pollington, A.D., Valley, J.W., 2014. Evolution of quartz cementation and burial history of the Eau Claire Formation based on in situ oxygen isotope analysis of quartz overgrowths. Chem. Geol. 384, 168–180. https://doi.org/10.1016/j.chemgeo.2014.06.021

Irwin, H., Curtis, C., Coleman, M., 1977. Isotopic evidence for source of diagenetic carbonates formed during burial of organic-rich sediments. Nat. 1977 2695625 269, 209–213. https://doi.org/10.1038/269209a0

Isaksen, D., Tonstad, K., 1989. A revised Cretaceous and Tertiary lithostratigraphic nomenclature for the Norwegian North Sea. NPD Bull. 5.

Jackson, C.A.L., Barber, G.P., Martinsen, O.J., 2008. Submarine slope morphology as a control on the development of sand-rich turbidite depositional systems: 3D seismic analysis of the Kyrre Fm (Upper Cretaceous), Måløy Slope, offshore Norway. Mar. Pet. Geol. 25, 663–680. https://doi.org/10.1016/J.MARPETGEO.2007.12.007

Jackson, J.A., 2012. Carbonate cementation in sandstones of the Plover Formation, North West Shelf, W.A.

Jaffrés, J.B.D., Shields, G.A., Wallmann, K., 2007. The oxygen isotope evolution of seawater: A critical review of a long-standing controversy and an improved geological water cycle model for the past 3.4 billion years. Earth-Science Rev. 83, 83–122. https://doi.org/10.1016/j.earscirev.2007.04.002

Kantorowicz, J.D., Bryant, I.D., Dawans, J.M., 1987. Controls on the geometry and distribution of carbonate cements in Jurassic sandstones: Bridport Sands, southern England and Viking Group, Troll Field, Norway. Geol. Soc. Spec. Publ. https://doi.org/10.1144/GSL.SP.1987.036.01.09

Krumbein, W.C. and L.L.S., 1963. Stratigraphy and Sedimentation (2nd Ed.). San Francisco: W.H. Freeman, 1963,.

Ku, T.C.W., Walter, L.M., 2003. Syndepositional formation of Fe-rich clays in tropical shelf sediments, San Blas Archipelago, Panama. Chem. Geol. 197, 197–213. https://doi.org/10.1016/S0009-2541(02)00363-7

Larson, R.L., 1991. Geological consequences of superplumes. Geology. https://doi.org/10.1130/0091-7613(1991)019<0963:GCOS>2.3.CO;2

Lawrence, M.G., Greig, A., Collerson, K.D., Kamber, B.S., 2006. Rare earth element and yttrium variability in South East Queensland waterways. Aquat. Geochemistry 12, 39–72. https://doi.org/10.1007/s10498-005-4471-8

Lee, S.G., Lee, D.H., Kim, Y., Chae, B.G., Kim, W.Y., Woo, N.C., 2003. Rare earth elements as indicators of groundwater environment changes in a fractured rock system: Evidence from fracture-filling calcite. Appl. Geochemistry. https://doi.org/10.1016/S0883-2927(02)00071-9

Lidmar-Bergström, K., Olsson, S., Roaldset, E., 2009. Relief Features and Palaeoweathering Remnants in Formerly Glaciated Scandinavian Basement Areas, in: Palaeoweathering, Palaeosurfaces and Related Continental Deposits. pp. 275–301. https://doi.org/10.1002/9781444304190.ch11

Lien, T., Midtbø, R.E., Martinsen, O.J., 2006. Depositional facies and reservoir quality of deep-marine sandstones in the Norwegian Sea. Nor. Geol. Tidsskr.

Lindholm, R.C., Finkelman, R.B., 1972. Calcite staining; semiquantitative determination of ferrous iron. J. Sediment. Res. https://doi.org/10.1306/74d724fa-2b21-11d7-8648000102c1865d

Liu, S.B., Huang, S.J., Shen, Z.M., Lü, Z.X., Song, R.C., 2014. Diagenetic fluid evolution and water-rock interaction model of carbonate cements in sandstone: An example from the reservoir sandstone of the Fourth Member of the Xujiahe Formation of the Xiaoquan-Fenggu area, Sichuan Province, China. Sci. China Earth Sci. https://doi.org/10.1007/s11430-014-4851-2

Longstaffe, Fred J, 2003. Berthierine, in: Middleton, G. V, Church, M.J., Coniglio, M., Hardie, L.A., Longstaffe, Frederick J (Eds.), Encyclopedia of Sediments and Sedimentary Rocks. Springer Netherlands, Dordrecht, pp. 64–66. https://doi.org/10.1007/978-1-4020-3609-5_26

Lundegard, P.D., 1992. Sandstone porosity loss; a big picture view of the importance of compaction. J. Sediment. Res. 62, 250–260. https://doi.org/10.1306/D42678D4-2B26-11D7-8648000102C1865D

Mansurbeg, H., Caja, M.A., Marfil, R., Morad, S., Remacha, E., Garcia, D., Martin-Crespo, T., El-Ghali, M.A.K., Nystuen, J.P., 2009. Diagenetic Evolution and Porosity Destruction of Turbiditic Hybrid Arenites and Siliciclastic Sandstones of Foreland Basins: Evidence from the Eocene Hecho Group, Pyrenees, Spain. J. Sediment. Res. https://doi.org/10.2110/jsr.2009.060

Mansurbeg, H., De Ros, L.F., Morad, S., Ketzer, J.M., El-Ghali, M.A.K., Caja, M.A., Othman, R., 2012. Meteoric-water diagenesis in late Cretaceous canyon-fill turbidite reservoirs from the Espírito Santo Basin, eastern Brazil. Mar. Pet. Geol.

https://doi.org/10.1016/j.marpetgeo.2012.03.009

Mansurbeg, H., Morad, S., Al Suwaidi, M., Qurtas, S., Tveiten, O.G., Shahrokhizadeh, S., Harchegani, F.K., 2020. Meteoric-water incursion into marine turbditic sandstones: Evidence from the Andrew Formation (Paleocene), UK Central Graben, North sea. Mar. Pet. Geol. 118, 104428. https://doi.org/https://doi.org/10.1016/j.marpetgeo.2020.104428

Martinsen, O.J., Lien, T., Jackson, C., 2005. Cretaceous and Palaeogene turbidite systems in the North Sea and Norwegian Sea basins: Source, staging area and basin physiography controls on reservoir development, in: Petroleum Geology Conference Proceedings. pp. 1147–1164. https://doi.org/10.1144/0061147

Matteo, E.N., Huet, B., Jové-Colón, C.F., Scherer, G.W., 2018. Experimental and modeling study of calcium carbonate precipitation and its effects on the degradation of oil well cement during carbonated brine exposure. Cem. Concr. Res. https://doi.org/10.1016/j.cemconres.2018.03.016

McLennan, S.M., 2001. Relationships between the trace element composition of sedimentary rocks and upper continental crust. Geochemistry, Geophys. Geosystems. https://doi.org/10.1029/2000GC000109

Moore, D.M., Reynolds, R.C. j., 1997. X-Ray Diffraction and the Identification and Analysis of Clay Minerals, second edition, Oxford University Press.

Morad, S., 1998. Carbonate Cementation in Sandstones: Distribution Patterns and Geochemical Evolution, in: Carbonate Cementation in Sandstones. John Wiley & Sons, Ltd, pp. 1–26. https://doi.org/https://doi.org/10.1002/9781444304893.ch1

Morad, S., de Ros, L.F., Nystuen, J.P., Bergan, M., 1996. Carbonate Diagenesis and Porosity Evolution in Sheet-Flood Sandstones: Evidence from the Middle and Lower Lunde Members (Triassic) in the Snorre Field, Norwegian North Sea, in: Carbonate Cementation in Sandstones. Blackwell Publishing Ltd., Oxford, UK, pp. 53–85. https://doi.org/10.1002/9781444304893.ch3

Mtys, J., 2009. Carbonate Cements in the Tertiary Sandstones of the Swiss Molasse Basin: Relevance to Palaeohydrodynamic Reconstruction, in: Carbonate Cementation in Sandstones. https://doi.org/10.1002/9781444304893.ch6

Mu, N., Schulz, H.M., Fu, Y., Schovsbo, N.H., Wirth, R., Rhede, D., van Berk, W., 2015. Berthierine formation in reservoir rocks from the Siri oilfield (Danish North Sea) as result of fluid-rock interactions: Part I. Characterization. Mar. Pet. Geol. 65, 302–316. https://doi.org/10.1016/j.marpetgeo.2015.04.010

Nothdurft, L.D., Webb, G.E., Kamber, B.S., 2004. Rare earth element geochemistry of Late Devonian reefal carbonates, Canning Basin, Western Australia: Confirmation of a seawater REE proxy in ancient limestones. Geochim. Cosmochim. Acta 68, 263–283. https://doi.org/10.1016/S0016-7037(03)00422-8

Nystuen, J.P., 1999. Submarine sediment gravity flow deposits and associated facies: core examples from the Agat Member, in: Extended Abstracts Bergen Conference. Norwegian Petroleum Society. pp. 211-215.

Oakman, C.D., Partington, M.A., 1998. Petroleum Geology of the North Sea, in: Cretaceous.In: GLENNIE, K.W. (Ed.) Petroleum Geology of the North Sea, Basic Concepts and Recent Advances, 4th Edn, Blackwell Scientific, Oxford, 294-349. pp. 294–349. https://doi.org/10.1016/s0037-0738(00)00100-7

Odin, G.S., 1988. Introduction to The Study of Green Marine Clays. Dev. Sedimentol. 45, 1–3. https://doi.org/10.1016/S0070-4571(08)70054-2

Olesen, O., Bering, D., Brönner, M., Dalsegg, E., Fabian, K., Fredin, O., Gellein, J., Husteli, B., Magnus, C., Rønning, J.S., Solbakk, T., J.F., T., J.A, Ø., 2012. NGU Report 2012.005 Tropical Weathering in Norway, TWIN Final Report 188.

Pe-Piper, G., Piper, D.J.W., 2020. Significance of the chemistry and morphology of diagenetic siderite in clastic rocks of the Mesozoic Scotian Basin. Sedimentology 67, 782–809. https://doi.org/10.1111/sed.12661

Pe-Piper, G., Weir-Murphy, S., 2008. Early diagenesis of inner-shelf phosphorite and iron-silicate minerals, lower cretaceous of the orpheus graben, southeastern Canada: Implication for the origin of chlorite rims. Am. Assoc. Pet. Geol. Bull. 92, 1153–1168. https://doi.org/10.1306/05050807118

Porrenga, D.H., 1967. Glauconite and chamosite as depth indicators in the marine environment. Mar. Geol. 5, 495–501. https://doi.org/10.1016/0025-3227(67)90056-4

Porten, K.W., Warchoł, M.J., Kane, I.A., 2019. Formation of detrital clay grain coats by dewatering of deep-water sands and significance for reservoir quality. J. Sediment. Res. 89, 1231–1249. https://doi.org/10.2110/jsr.2019.65

Prosser, D.J., Daws, J.A., Fallick, A.E., Williams, B.P.J., 1993. Geochemistry and diagenesis of stratabound calcite cement layers within the Rannoch Formation of the Brent Group, Murchison Field, North Viking Graben (northern North Sea). Sediment. Geol. https://doi.org/10.1016/0037-0738(93)90002-M

Riis, F., Wolff, A., 2020. Use of pore pressure data from the Norwegian Continental Shelf to characterize fluid-flow processes in geological timescales. Geol. Soc. London, Spec. Publ. SP495-2018–176. https://doi.org/10.1144/SP495-2018-176

Roduit, N., 2007. un logiciel d’analyse d’images pétrographiques polyvalent.

Ryan, P.C., Hillier, S., 2002. Berthierine/chamosite, corrensite, and discrete chlorite from evolved verdine and evaporite-associated facies in the Jurassic Sundance Formation, Wyoming. Am. Mineral. 87, 1607–1615. https://doi.org/10.2138/am-2002-11-1210

Saïag, J., Brigaud, B., Portier, É., Desaubliaux, G., Bucherie, A., Miska, S., Pagel, M., 2016. Sedimentological control on the diagenesis and reservoir quality of tidal sandstones of the Upper Cape Hay Formation (Permian, Bonaparte Basin, Australia). Mar. Pet. Geol. 77, 597–624. https://doi.org/10.1016/j.marpetgeo.2016.07.002

Saigal, G.C., Bjørlykke, K., 1987. Carbonate cements in clastic reservoir rocks from offshore Norway-relationships between isotopic composition, textural development and burial depth. Geol. Soc. Spec. Publ. 36, 313–324. https://doi.org/10.1144/GSL.SP.1987.036.01.22

Saigal, G.C., Morad, S., Bjorlykke, K., Egeberg, P.K., Aagaard, P., 1988. Diagenetic albitization of detrital K-feldspar in Jurassic, Lower Cretaceous, and Tertiary clastic reservoir rocks from offshore Norway, I. Textures and origin. J. Sediment. Petrol. 58, 1003–1013. https://doi.org/10.1306/212F8EE5-2B24-11D7-8648000102C1865D

Schmidt, V., Mcdonald, D.A., 1979. Texture and Recognition of Secondary Porosity in Sandstones. Asp. Diagenes. 209–225. https://doi.org/10.2110/PEC.79.26.0209

Schultz, J.L., Boles, J., Tilton, G.R., 1989. Tracking calcium in the San Joaquin basin, California: A strontium isotopic study of carbonate cements at North Coles Levee. Geochim. Cosmochim. Acta 53, 1991–1999. https://doi.org/10.1016/0016-7037(89)90319-0

Shanmugam, G., 1995. Basin-floor fans in the North Sea: sequence stratigraphic models vs. sedimentary facies. Am. Assoc. Pet. Geol. Bull. 79, 477–512. https://doi.org/10.1306/8d2b1570-171e-11d7-8645000102c1865d

Shanmugam, G., Lehtonen, L.R., Straume, T., Syvertsen, S.E., Hodgkinson, R.J., Skibeli, M., 1994. Slump and debris-flow dominated upper slope facies in the Cretaceous of the Norwegian and northern North Seas (61-67°N): implications for sand distribution. Am. Assoc. Pet. Geol. Bull. https://doi.org/10.1306/a25fe3e7-171b-11d7-8645000102c1865d

Skibeli, M., Barnes, K., Straume, T., Syvertsen, S.E., Shanmugam, G., 1995. A sequence stratigraphic study of lower cretaceous deposits in the northernmost North Sea. Nor. Pet. Soc. Spec. Publ. 5, 389–400. https://doi.org/10.1016/S0928-8937(06)80077-9

Steele-MacInnis, M., Lecumberri-Sanchez, P., Bodnar, R.J., 2012. HokieFlincs_H2O-NaCl: A Microsoft Excel spreadsheet for interpreting microthermometric data from fluid inclusions based on the PVTX properties of H 2O-NaCl. Comput. Geosci. 49, 334–337. https://doi.org/10.1016/j.cageo.2012.01.022

Surdam, R.C., Crossey, L.J., Hagen, E.S., Heasler, H.P., 1989. Organic-inorganic interactions and sandstone diagenesis. Am. Assoc. Pet. Geol. Bull. https://doi.org/10.1306/703c9ad7-1707-11d7-8645000102c1865d

Taylor, J., 1950. Pore-Space Reduction in Sandstones. Am. Assoc. Pet. Geol. Bull. 34, 701–716.

Taylor, K.G., Macquaker, J.H.S., 2011. Iron minerals in marine sediments record chemical environments. Elements 7, 113–118. https://doi.org/10.2113/gselements.7.2.113

Tostevin, R., Shields, G.A., Tarbuck, G.M., He, T., Clarkson, M.O., Wood, R.A., 2016. Effective use of cerium anomalies as a redox proxy in carbonate-dominated marine settings. Chem. Geol. https://doi.org/10.1016/j.chemgeo.2016.06.027

Van Houten, F.B., Purucker, M.E., 1984. Glauconitic peloids and chamositic ooids - favorable factors, constraints, and problems. Earth Sci. Rev. 20, 211–243. https://doi.org/10.1016/0012-8252(84)90002-3

Verhagen, I.T.E., Crisóstomo-Figueroa, A., Utley, J.E.P., Worden, R.H., 2020. Abrasion of detrital grain-coating clays during sediment transport: Implications for diagenetic clay coats. Sediment. Geol. 403, 105653. https://doi.org/10.1016/j.sedgeo.2020.105653

Virolle, M., Brigaud, B., Beaufort, D., Patrier, P., Abdelrahman, E., Thomas, H., Portier, E., Samson, Y., Bourillot, R., Féniès, H., 2022. Authigenic berthierine and incipient chloritization in shallowly buried sandstone reservoirs: Key role of the source-to-sink context. GSA Bull. https://doi.org/10.1130/b35865.1

Virolle, M., Brigaud, B., Bourillot, R., Féniès, H., Portier, E., Duteil, T., Nouet, J., Patrier, P., Beaufort, D., 2019. Detrital clay grain coats in estuarine clastic deposits: origin and spatial distribution within a modern sedimentary system, the Gironde Estuary (south-west France). Sedimentology 66, 859–894. https://doi.org/10.1111/sed.12520

Virolle, M., Féniès, H., Brigaud, B., Bourillot, R., Portier, E., Patrier, P., Beaufort, D., Jalon-Rojas, I., Derriennic, H., Miska, S., 2020. Facies associations, detrital clay grain coats and mineralogical characterization of the Gironde estuary tidal bars: A modern analogue for deeply buried estuarine sandstone reservoirs. Mar. Pet. Geol. 114, 104225. https://doi.org/10.1016/j.marpetgeo.2020.104225

Wetzel, A., 1993. The transfer of river load to deep-sea fans: a quantitative approach. Am. Assoc. Pet. Geol. Bull. 77. https://doi.org/10.1306/bdff8efc-1718-11d7-8645000102c1865d

Wilkinson, M., Haszeldine, R.S., Fallick, A.E., Osborne, M.J., 2000. Siderite zonation within the Brent Group: microbial influence or aquifer flow? Clay Miner. 35, 107–117. https://doi.org/10.1180/000985500546512

Wilkinson, M., Milliken, K.L., Haszeldine, R.S., 2001. Systematic destruction of K-feldspar in deeply buried rift and passive margin sandstones. J. Geol. Soc. London. 158, 675–684. https://doi.org/10.1144/jgs.158.4.675

Wooldridge, L.J., Worden, R.H., Griffiths, J., Thompson, A., Chung, P., 2017. Biofilm origin of clay-coated sand grains. Geology 45, 875–878. https://doi.org/10.1130/G39161.1

Wooldridge, L.J., Worden, R.H., Griffiths, J., Utley, J.E.P., 2019. Clay-coat diversity in marginal marine sediments. Sedimentology 66, 1118–1138. https://doi.org/10.1111/sed.12538

Worden, R.., Griffiths, J., Wooldridge, L.., Utley, J.E.., Lawan, A.., Muhammed, D.., Simon, N., Armitage, P.., 2020. Chlorite in sandstones. Earth-Science Rev. 204, 103105. https://doi.org/10.1016/j.earscirev.2020.103105

Worden, R.H., Burley, S.D., 2003. Sandstone Diagenesis: The Evolution of Sand to Stone, in: Sandstone Diagenesis. John Wiley & Sons, Ltd, pp. 1–44. https://doi.org/https://doi.org/10.1002/9781444304459.ch

Worden, R.H., Griffiths, J., Wooldridge, L.J., Utley, J.E.P., Lawan, A.Y., Muhammed, D.D., Simon, N., Armitage, P.J., 2020. Chlorite in sandstones. Earth-Science Rev. 204, 103105. https://doi.org/10.1016/j.earscirev.2020.103105

Worden, R.H., Morad, S., 2000. Quartz Cementation in Oil Field Sandstones: A Review of the Key Controversies, in: Quartz Cementation in Sandstones. John Wiley & Sons, Ltd, pp. 1–20. https://doi.org/https://doi.org/10.1002/9781444304237.ch1

Worden, R.H., Morrall, G.T., Kelly, S., Mc Ardle, P., Barshep, D. V., 2019. A renewed look at calcite cement in marine-deltaic sandstones: the Brent Reservoir, Heather Field, northern North Sea, UK. Geol. Soc. London, Spec. Publ. SP484-2018–43. https://doi.org/10.1144/sp484-2018-43

Xia, H., Perez, E.H., Dunn, T., 2020. The impact of grain-coating chlorite on the effective porosity of sandstones. Mar. Pet. Geol. 104237. https://doi.org/10.1016/j.marpetgeo.2020.104237

Xiong, D., Azmy, K., Blamey, N.J.F., 2016. Diagenesis and origin of calcite cement in the Flemish Pass Basin sandstone reservoir (Upper Jurassic): Implications for porosity development. Mar. Pet. Geol. 70, 93–118. https://doi.org/10.1016/j.marpetgeo.2015.11.013

Yezerski, D.J., Shumaker, N., 2018. PS Improving Prediction of Porosity Preservation in Thermally-Stressed Deep Marine Sandstones: A Synthesis of Grain-Coating Chlorite Observations*, in: AAPG 2017 Annual Convention and Exhibition.

Yuan, G., Cao, Y., Jia, Z., Gluyas, J., Yang, T., Wang, Y., Xi, K., 2015. Selective dissolution of feldspars in the presence of carbonates: The way to generate secondary pores in buried sandstones by organic CO2. Mar. Pet. Geol. 60, 105–119. https://doi.org/10.1016/j.marpetgeo.2014.11.001

Yuan, G., Cao, Y., Schulz, H.M., Hao, F., Gluyas, J., Liu, K., Yang, T., Wang, Y., Xi, K., Li, F., 2019. A review of feldspar alteration and its geological significance in sedimentary basins: From shallow aquifers to deep hydrocarbon reservoirs. Earth-Science Rev. https://doi.org/10.1016/j.earscirev.2019.02.004

Yuan, G., Cao, Y., Zhang, Y., Gluyas, J., 2017. Diagenesis and reservoir quality of sandstones with ancient “deep” incursion of meteoric freshwater——An example in the Nanpu Sag, Bohai Bay Basin, East China. Mar. Pet. Geol. https://doi.org/10.1016/j.marpetgeo.2017.02.027

Zhang, J., Nozaki, Y., 1996. Rare earth elements and yttrium in seawater: ICP-MS determinations in the East Caroline, Coral Sea, and South Fiji basins of the western South Pacific Ocean. Geochim. Cosmochim. Acta. https://doi.org/10.1016/S0016-7037(96)00276-1

Zhang, Y., Zeng, J., Yu, B., 2009. Experimental study on interaction between simulated sandstone and acidic fluid. Pet. Sci. 6, 8–16. https://doi.org/10.1007/s12182-009-0002-3

Zheng, Y.F., 1999. Oxygen isotope fractionation in carbonate and sulfate minerals. Geochem. J. 33, 109–126. https://doi.org/10.2343/geochemj.33.109

Zheng, Y.F., 1993. Calculation of oxygen isotope fractionation in hydroxyl-bearing silicates. Earth Planet. Sci. Lett. 120, 247–263. https://doi.org/10.1016/0012-821X(93)90243-3

Ziegler, P.A., 1992. North Sea rift system. Tectonophysics 208, 55–75. https://doi.org/https://doi.org/10.1016/0040-1951(92)90336-5

Ziegler, P.A., 1975. Geologic Evolution of North Sea and Its Tectonic Framework. Am. Assoc. Pet. Geol. Bull. 59, 1073–1097. https://doi.org/10.1306/83D91F2E-16C7-11D7-8645000102C1865D